

Measurement of Temperature, Refractive Index, or Axial Acceleration with Etched PCF Microfiber Structure

Brennan N. Thews

Thesis submitted to the Faculty of the
Virginia Polytechnic Institute and State University
in partial fulfillment of the requirements for the degree of

Master of Science
in
Electrical and Computer Engineering

Anbo Wang, Chair
Yong Xu
Ahmed Safaai-Jazi

June 22, 2015
Blacksburg, Virginia

Keywords: Etched PCF, IFPI Cavity, Microfiber, Cantilever Beam

Copyright 2015, Brennan N. Thews

Measurement of Temperature, Refractive Index, or Axial Acceleration with Etched PCF Microfiber Structure

Brennan N. Thews

(ABSTRACT)

In the field of optical fiber sensors, one of the most versatile structures is the Fabry-Perot interferometer. This thesis will present a novel sensor based on an Intrinsic Fabry-Perot Interferometer (IFPI) cavity to measure axial acceleration, refractive index, and temperature. The sensor structure is based on previous work done by R. Wang at the Center for Photonics Technology. This work suggests its flexibility in many different roles with a sensitivity to axial acceleration of $70 \text{ pm}/\text{unit of acceleration}$, to refractive index of $60 \text{ nm}/\text{Refractive Index Unit}$, and to temperature of $7.8 \text{ pm}/^\circ\text{C}$. Future work is also discussed in measuring tangential acceleration with direction using a PM fiber as the lead-in and observing the reflections on the slow and fast axes.

Dedication

I would like to dedicate this dissertation to my family. To my late father Eric, my mother Karen, and my brother Jonathan. I appreciate all you have done for me on this journey and am glad I had a support system as strong as you. I'd also like to thank the second half of that support system, the friends I have made previously and after coming to Virginia Tech, specifically Kenneth Morgan, Matthew Shipton, and Paul David. You were always there to brighten my day even on the worst of them.

Acknowledgments

I would like to first and foremost acknowledge my advisor Dr. Wang. His patience and advice through this process was invaluable. I'd also like to acknowledge the Center for Photonics Technology in general. The lab is filled with smart, dedicated students who are more than willing to discuss topics and explain abstract concepts without it needing to pertain to their own research. Specifically, I'd like to acknowledge Matthew Shipton and Michael Fraiser for both their help in constructing testing schemes and for keeping me on track to the finish line.

Contents

1	Previous Work	1
1.1	Optical Fiber Sensors	1
1.2	Temperature Sensors	4
1.3	Refractive Index Sensors	5
1.4	IFPI Sensors	6
1.5	Vibration Sensors	8
2	Basic Principles	12
2.1	Types of Fiber	12
2.1.1	Single-Mode Fiber	12
2.1.2	Panda-Style Polarization Maintaining Fiber	15
2.1.3	Photonic Crystal Fiber	17
2.2	IFPI Cavities	19
2.3	Cantilever Beams	25
2.4	Macrobanding	29

3	Sensor Structure	31
3.1	Fabrication	31
3.1.1	Pre-etching Fiber Parameters	31
3.1.2	Etching Considerations	34
3.2	IFPI Performance	38
3.2.1	SMF Case	38
3.2.2	PMF Case	41
4	Testing	43
4.1	Temperature Testing	43
4.2	External Refractive Index Testing	46
4.3	Axial Acceleration Testing	48
5	Future Work	53
5.1	Work done on Tangential Acceleration	53
5.2	Other areas to explore	58
6	Concluding Remarks	59
	Bibliography	60
A	Axial vibration testing	66

List of Figures

1.1	Models of the (a) extrinsic and (b) intrinsic cases of an FP interferometer. . .	3
1.2	Fabry-Perot Cavity micromachined by Pevec and Donlagic [31] Used under fair use, 2015	7
1.3	Structure of etched PCF cavity from R. Wang [36] Used under fair use, 2015	8
1.4	Structure of FBG vibration sensor presented by Theriault [41] Used under fair use, 2015	9
1.5	Vibration sensor using fiber-to-fiber coupling presented by Malki [45] Used under fair use, 2015	10
1.6	IFPI sensor using the(a) transmission technique and (b) reflection technique [47] Used under fair use, 2015	11
2.1	Structure of a SMF with core, cladding, and coating and typical values . . .	13
2.2	Total internal reflection	15
2.3	Structure of Panda-Style PMF	16
2.4	Structure of a PCF showing the core and holey cladding	17
2.5	Typical attenuation and dispersion curves for PCF	18
2.6	Fabry-Perot etalon structure	20

2.7	Uniformly distributed load cantilever beam	25
2.8	Displacement of cantilever beam under load	27
2.9	Radius of curvature for a cantilever beam under load	29
3.1	ESM-12B PCF end	32
3.2	ESM-12B PCF side view	34
3.3	SMF etching progression	35
3.4	SMF etching after 195 s for (a) 100 μm , (b) 150 μm , and (c) 200 μm length cavities	36
3.5	PMF etching progression	37
3.6	SMF etching progression	38
3.7	Spectrum with different cavity lengths	40
3.8	PMF spectrum after etching	41
4.1	Temperature testing setup	44
4.2	Temperature testing results	45
4.3	Temperature testing FSR results	46
4.4	External refractive index testing results	47
4.5	External refractive index FSR results	48
4.6	Axial acceleration testing setup	49
4.7	Axial acceleration fiber placement	50
4.8	Axial vibration results	51

5.1	FFT of building vibrations	54
5.2	Setup of tangential vibration test	55
5.3	Slow mode tangential to acceleration direction	56
5.4	PMF tangential vibration results	57
A.1	Axial vibration at 50 RPM	66
A.2	Spectrum of axial vibration at 50 RPM	67
A.3	Axial vibration at 75 RPM	67
A.4	Spectrum of axial vibration at 75 RPM	68
A.5	Axial vibration at 100 RPM	68
A.6	Spectrum of axial vibration at 100 RPM	69
A.7	Axial vibration at 125 RPM	69
A.8	Spectrum of axial vibration at 125 RPM	70
A.9	Axial vibration at 150 RPM	70
A.10	Spectrum of axial vibration at 150 RPM	71
A.11	Axial vibration at 175 RPM	71
A.12	Spectrum of axial vibration at 175 RPM	72
A.13	Axial vibration at 200 RPM	72
A.14	Spectrum of axial vibration at 200 RPM	73

Chapter 1

Previous Work

1.1 Optical Fiber Sensors

Optical fiber sensors have a rich history that stretches back to the development of optical fibers, dating back to the "fotonic" sensor in the late 1960's [1]. Although, what started off as two bundles of fiber sensing distance has since evolved in leaps and bounds, spilling over into many other fields and providing a significant impact on technology today. Today, optical fiber sensors are ubiquitous throughout every sector, found in industry [2–5], medicine [6–8], and everything in between.

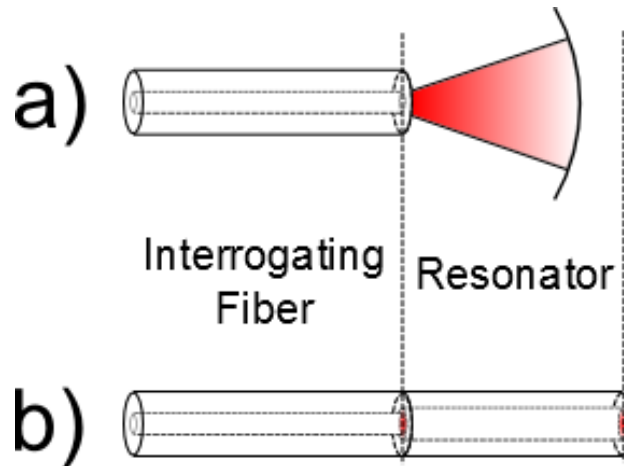
Sensors which utilize optical fiber have many advantages over other technologies. One of the biggest examples of this is their immunity to electromagnetic interference (EMI). These sensors can operate in large dynamic electric fields without significantly impacting their measurements. Their small form factor can be useful in projects where space is a premium, such as on space missions. The high sensitivity and bandwidth of these sensors gives them a distinct advantage over alternatives. A main ability of fiber sensors is their ability to be used in distributed and multiplexed networks. In these networks a single source is able to interrogate many sensors, even numbering in the hundreds, with a single pulse and distinguish

each sensor individually from the returned signal. Finally, no moving mechanical parts means that there are less points of failure the system and, due to the optical telecommunications industry, the cost for optical fiber is decreasing.

Although optical fiber sensors are found in so many fields, most of the sensors produced are application-specific with each market sector having their own particular requirements [9] due to the broadness of the field and the many methods used to interrogate mediums. A non-exhaustive list of some of these methods would be the Mach-Zender Interferometer, Sagnac interferometer, Michaelson Interferometer, Fiber Bragg Grating, Faraday Rotation, Brillouin and Raman Scattering, Gas Spectroscopy, and Fabry-Perot etalon based sensors. Due to the nature of this thesis, Fabry-Perot etalon based sensors will be the main method studied.

Charles Fabry and Alfred Perot first developed their interferometer back in 1897 with their first publication [10]. They saw its usefulness in the study of spectroscopy, meteorology and astrophysics, publishing 15 papers on the topic between 1897 and 1902 [11]. Since then, Fabry-Perot (FP) interferometers have become an integral part of many sensing systems. With respect to sensors, however, FP interferometry setups fall into two categories: extrinsic and intrinsic. These categories are fundamentally different. Figure 1.1 shows the difference graphically.

Figure 1.1: Models of the (a) extrinsic and (b) intrinsic cases of an FP interferometer.



In the extrinsic case, light guided through an optical fiber is launched into a fiber for measuring, which can either be the same or a different fiber. In this method, the interaction region outside of the fiber is measured [12]. When the light is launched out of the fiber, the medium it travels through modulates the light based on physical properties such as changing its amplitude, wavelength, polarization or phase. In the case shown in Figure 1.1, the cavity is in free-space with air or some other medium in between two mirrored surfaces. A cleaved fiber end is represented as a mirrored surface. When the light is recoupled into a fiber and detected or impinges onto a free-space detector, the changes to the light can be observed and extracted. The full explanation of FP resonators is given in Section 2.2. Examples of extrinsic sensors would be to measure varying strain [13], temperature [14], and the level of a liquid [15].

Conversely, intrinsic sensors use properties inherent to the fiber to discover properties about the outside environment without any light leaving the fiber. In the extrinsic case (Figure 1.1a), there were external mirrors to create the cavity. In the intrinsic case (Figure 1.1b), the fiber itself is modified so that it has cavity-like properties without any free-space coupling. This allows the measurement of mediums that interact with the fiber with higher coupling

efficiency and, therefore, possibly higher sensitivity. Intrinsic sensors are becoming more common than extrinsic sensors and include examples such as measuring refractive index and temperature simultaneously [16], pressure [17], and for intracellular measurements [18]. The range of applications that the FP interferometer can be applied to makes it one of the most versatile sensing methods.

1.2 Temperature Sensors

Temperature sensing is one of the most commercially available and heavily researched areas of optical sensors. There are many methods of sensing temperature that are used both commercially and in the lab setting including: FP interferometers [16, 19–22], black body radiation [23], Raman scattering monitoring [24], and fluorescence monitoring [25]. All of these fields have been fairly well examined and now temperature is usually a secondary measurement. With FP interferometry, the temperature usually affects the length of the cavity, causing the cavity to stretch or compress based on temperature fluctuations. This causes the resulting reflected spectrum to shift based on the cavity change. Measuring blackbody radiation is fairly straightforward. A blackbody cavity is created at the tip of the sensor and the light it gives off is coupled into fiber. Then, based on the amplitude and frequency of the signal, the temperature can be discerned. Using Raman scattering, the back-reflected light is shifted due to a change in temperature; usually, a pulse is sent down a sensing fiber and the Raman scattering reflections are measured. The amplitude of these reflections depend on the temperature and the loss of the fiber at that location. Fluorescence monitoring is based on the temperature dependent variation in light transmission that occurs through certain transparent substances.

1.3 Refractive Index Sensors

In terms of refractive index sensors, the field is much less explored than with temperature. However, there are still many methods for discerning the refractive index. Some examples would be: using microfiber [26], long period gratings (LPGs) [27], or fluid-filled channels [28]. In all of these methods, the refractive index is measured based on the change in the propagation constant through the interrogated section.

Microfiber systems use the fact that when a fiber is drawn to a small diameter, some of the power leaks out of the cladding and into the surrounding area. When this occurs, the propagation constant, which is only a function of the core and cladding refractive indices, is now also a function of the surrounding refractive index. This additional parameter changes the effective refractive index through that section of the fiber, which can be measured through viewing the resulting spectrum.

LPGs are periodic changes in the core's refractive index which happen on an order much longer than the wavelength of light, typically a fraction of a mm. They are used to couple modes from the core to the cladding when they have similar propagation constants. Because they couple light into a cladding mode, some of the cladding mode light leaks into the surrounding area, thus the same principle as with the microfiber occurs and the propagation constant is changed and interrogated through processing.

Fluid filled channels are the main concern for this thesis. In the work done for this thesis, different refractive indices are placed inside a cavity and the resulting spectrum is discerned. This is similar to what was done by Wu [28] who used Photonic Crystal Fiber (PCF) and filled sections of its air holes with different analytes to change the propagation constant: this thesis work differs as it uses an IFPI cavity.

1.4 IFPI Sensors

It can be expected that due to the flexible nature of IFPI sensors there are many structural varieties. The main ways to fabricate an IFPI sensor including using Fiber Bragg Gratings (FBGs) to create a cavity between the gratings or to splice fibers of differing characteristics together to create the same effect.

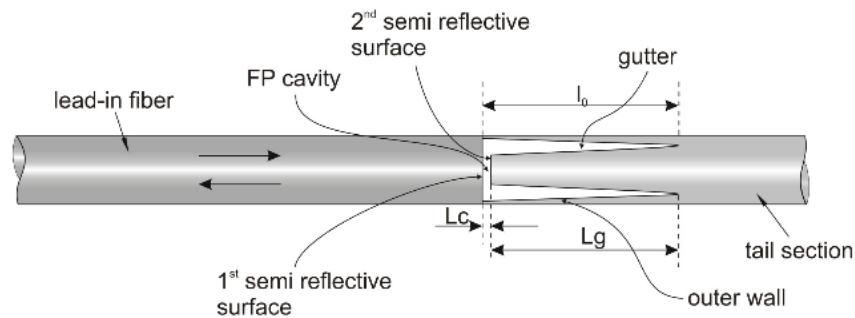
FBGs are periodic changes in the refractive index of the core which cause certain wavelengths to be reflected based on the Bragg condition. In the case of an IFPI sensor, two FBGs can be placed next to each other to create an FP structure. If the gratings are close enough together, a resonance will form between the gratings as light is partially reflected between them. This method has been used to create sensors for measuring temperature [19], strain [29], and even the two simultaneously [20]. Fabricating FP cavities this way is simple, effective, and has been used in many different arrangements and distributed systems.

The other main way of creating an IFPI sensor is to splice two fibers of varying characteristics together, creating reflections at the splicing points or end faces of the fibers. An example of this is shown in Figure 1.1b. When light is directed down the smaller-core fiber, at the point of core discontinuity there is a degree of reflection; the transmitted portion of the light continues to travel into the larger core and likewise gets partially reflected off of the fiber end face. This structure causes the larger-core fiber to act as an optical cavity. The interrogation, or lead-in, fiber usually consists of a single-mode fiber (SMF), polarization-maintaining fiber (PMF), or multi-mode fiber (MMF), however, the interferometer section can be many different types of fiber to measure different qualities. To measure pressure or strain, a hollow-core fiber may be used since they elongate as the measurand increases [30]. For temperature, SMF with different core diameters and refractive indices can be spliced together to make one side of the cavity and use the open air end of the fiber as the second reflection face [21]. Also, dielectric mirrors can be inserted into the splicing points to create the FP cavity such as for temperature sensing [22]. Interesting fiber structures are also being developed for this application, such as the strain sensor micromachined by Pevec and

Donlagic [31] and shown in Figure 1.2.

Figure 1.2: Fabry-Perot Cavity micromachined by Pevec and Donlagic

S. Pevec and D. Donlagic, "All-fiber, long-active-length fabry-perot strain sensor," *Optics express*, vol. 19, no. 16, pp. 15641-15651, 2011. Used under fair use, 2015



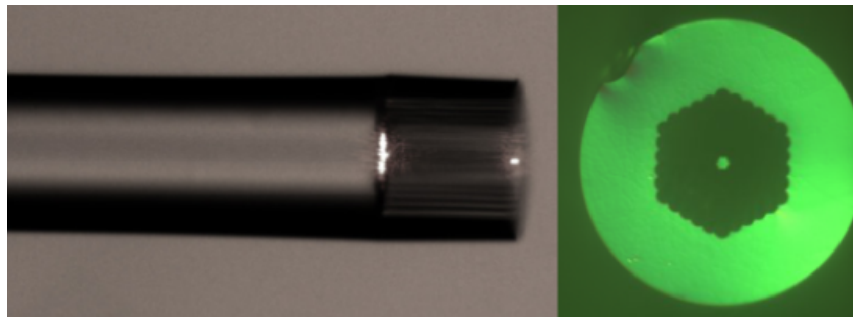
Due to the scope of this thesis, however, this work will focus on creating an FP cavity by splicing PCF onto the interrogation fiber, however, even narrowing down to only using PCF there are multiple ways to create the interferometer. A hollow-core PCF can be used to create a cavity [32], the PCF can be spliced in such a way that an air bubble forms at the splicing point [33], or using a regular PCF spliced to the end of the lead-in fiber [34]. There is also the method of creating a cavity which was first proposed by R. Wang in 2014 [35]. Wang creates an FP cavity by splicing a PCF to an SMF and then etching out the air-hole cladding to leave only the core. At the end of the etching process, the core is at microfiber thickness. This structure is interesting because it is shown to have increased fringe resolution over a normal SMF-PCF FP cavity and it leaves a microfiber suspended in a structure with its outer casing intact, protecting the fragile core.

R. Wang's work on this structure consists of three publications [35–37]. The first two of these discuss the temperature sensitivity of this sensor, while the third examines the structure for whispering-gallery mode excitation. All of the papers discuss the etching process and the specific characteristics of the fiber that was used as the cavity. This structure, shown in

Figure 3, will be the structural basis of this thesis topic.

Figure 1.3: Structure of etched PCF cavity from R. Wang

R. Wang and X. Qiao, "Micro fabry-perot interferometer based on suspended core created by etching microstructure fiber," in *OFS2014 23rd International Conference on Optical Fiber Sensors*, pp. 915780-915780, International Society for Optics and Photonics, 2014. Used under fair use, 2015



As shown above, the previous work done on this structure resulted with a microfiber core encased by a silica buffer. At the end of etching, Wang's structure included a core of about $3\mu\text{m}$ in diameter for a length of $100\mu\text{m}$. When testing, he found that this structure has a sensitivity to temperature of $14.3\text{pm}/^\circ\text{C}$. Another interesting aspect to this structure is that due to the length and diameter of the freestanding core, it acts like a uniformly-loaded cantilever beam.

1.5 Vibration Sensors

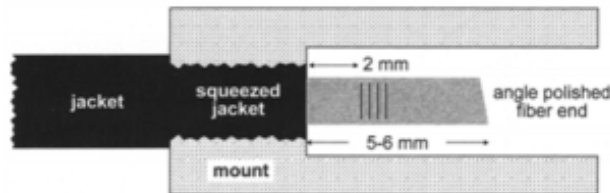
Cantilever beams have a niche place in optical fiber sensing, including in IFPI sensors. The main use of the core as a cantilever beam in optical sensing is for vibration, force, and acceleration detection due to their structure. Most of the other uses found were using optical sensors to observe metallic cantilever beams. These examples include finding the

level of a liquid [38], dampening the vibration of a cantilever beam [39], or imaging silicon cantilever beams for chemical sensing [40]. However, these systems are usually extrinsic systems whereas this thesis is about intrinsic structures.

In terms of vibration sensing, cantilever beams are usually used as the sensing element. An early example of this would be by Theriault in 1997 [41]. This sensor uses an FBG near the base of a 1 cm long cantilever beam, shown in Figure 1.4.

Figure 1.4: Structure of FBG vibration sensor presented by Theriault

S. Theriault, et al., "High-g accelerometer based on an in-fiber bragg grating sensor," *Optical Review*, vol. 4, no. 1, pp. A145-A147, 1997. Used under fair use, 2015



During axial acceleration the beam will compress, forcing the FBG's reflection spectrum to shift. Originally, the compression of the FBG would be non-uniform, however, the authors subvert this dilemma by creating a very short FBG with respect to the length of the beam, allowing it to be as a uniform compression. With this sensor, it was shown that the wavelength shift was linear up to the highest measurement of 1.7×10^5 times earth gravity.

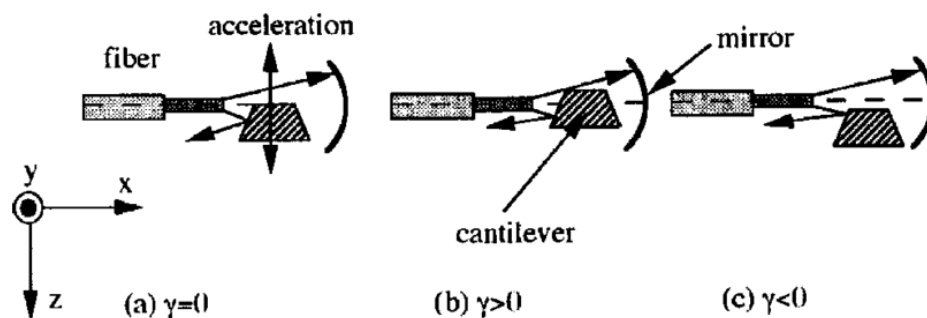
An interesting example would be using a bilateral cantilever beam with an FBG inserted at the middle and bonded to a fixed point [42]. With this structure, it was found that when a force was applied to both sides of the beam, depending on the direction of the force, the FBG would either stretch or compress leading to a red shift or blue shift of the resulting spectrum, respectively. In these experiments, the bilateral cantilever beam was subjected to a force at either end of the beam in opposite directions. This led to a broadening of the spectrum centered at the original FBG peak.

There is also a class of vibration sensing utilizing amplitude detection to detect vibration intensity. These sensors use techniques such as: fiber microbending, fiber-to-fiber coupling, moving gratings, and modified cladding [43]. Of these techniques, fiber-to-fiber coupling uses cantilever beams as a base for their structure. The basic principle of using fiber-to-fiber coupling is that two fibers are aligned for maximum light transmission and one of the fibers is set up as a cantilever beam while the other is fixed in place [44]. As the system is vibrated, the fibers misalign and there is a drop in the transmitted power. This change in the transmitted power can therefore be related to the acceleration of the fiber at its tip. This method will give tangential acceleration without direction.

In 1995 an article was published on the issue of using fiber-to-fiber coupling by Malki et. al. [45]; a fiber was placed in a v-groove with a mirrored cantilever beam in front of it at an angle and a concave mirror behind the cantilever focused at the fiber tip. When the cantilever beam is vibrated, the amount of light that is reflected back off the mirror changes, as shown in Figure 1.5.

Figure 1.5: Vibration sensor using fiber-to-fiber coupling presented by Malki

A. Malki, et. al, "Optical fiber accelerometer based on a silicon micromachined cantilever.," *Applied Optics*, vol. 34, no. 34, pp. 8014-8018, 1995. Used under fair use, 2015



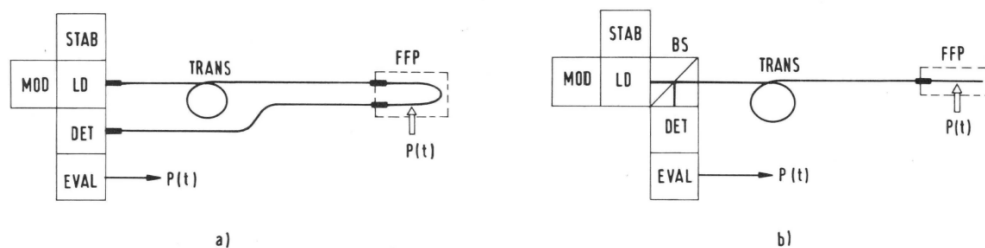
Therefore, when the force intensity on the cantilever is increased in the -z direction, less

light will be reflected back into the fiber. The opposite happens when the force is in the $+z$ direction.

IFPI structures are also prevalent in acceleration testing. This structure was first used as a vibration testing implement in 1982 by Yoshino when he was finding applications of IFPI in optical fibers [46]. When striking the bench the IFPI sensor was placed on, he saw phase modulation in the output signal for both single-mode and two-mode fiber.

In 1985, Kist et. al. [47] showed how to create an IFPI sensor for both transmission and reflection configurations for strain sensing, shown in Figure 1.6.

Figure 1.6: IFPI sensor using the(a) transmission technique and (b) reflection technique
 R. Kist, et al., "The fiber fabry-perot and its applications as a fiber-optic sensor element.,"
1986 International Technical Symposium/Europe, pp. 126-135, International Society for
 Optical and Photonics, 1986. Used under fair use, 2015



With these two configurations, Kist chose the transmission technique using graded-index fiber (GIF) as the cavity attached by ferrules to MMF. The GIF is then attached in a U-shape to a metal cantilever beam. By turning on an electromagnet under the beam, the fiber is strained, creating a larger cavity which can be seen in the resulting interference pattern.

As for using IFPI sensors in conjunction with cantilever beams for vibration detection, there are no direct references on the subject. This means that the structure presented by Wang is unique for application in both axial and tangential accelerations.

Chapter 2

Basic Principles

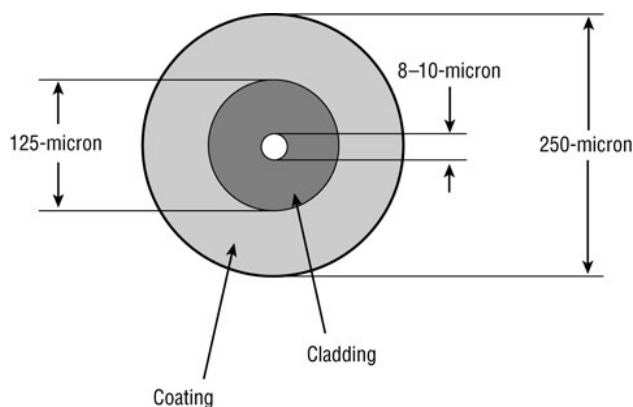
2.1 Types of Fiber

In this thesis, three types of fiber are used: Single-Mode Fiber (SMF), Panda-Style Polarization Maintaining Fiber (PMF), and Photonic Crystal Fiber (PCF). There are two iterations of the final design presented, the first with SMF and PCF to measure temperature, refractive index, and axial acceleration and the second with PMF and PCF to test tangential acceleration. This section explains how SMF, PMF, and PCF work and each of their unique characteristics.

2.1.1 Single-Mode Fiber

Single-Mode Fiber is a basic building block of many optical sensors and fiber optic networks that are in use and being developed today. The structure and dimensions of a basic SMF is shown in Figure 2.1.

Figure 2.1: Structure of a SMF with core, cladding, and coating and typical values



The basic SMF core and cladding consists of cylindrically symmetrical layers made from silica with different refractive indices and a coating around both for stability. Typically, the core diameter of SMF is between 8 and $10\mu m$ and the cladding diameter can be anywhere from $80\mu m$ up to $250\mu m$. The coating has no fixed dimensions since it changes based on what kind of environment the SMF is fabricated to withstand.

Focusing on step-index SMF, only one mode can propagate through the fiber due to its small V-number. The V-number in a SMF, also known as the normalized frequency, must be less than 2.4048 to only let one mode propagate in the fiber. The equation for the V-number is given as:

$$V = \frac{2\pi a_f}{\lambda} \sqrt{n_1^2 - n_2^2} = \frac{2\pi a_f}{\lambda} NA \quad (2.1)$$

where λ is the wavelength in the medium, NA is the numerical aperture of the fiber, a_f is the radius of the core, and n_1 and n_2 are the indexes of refraction for the core and cladding, respectively. Interestingly, the single-mode cutoff V-number of 2.4048 is also the first root of the Bessel function J_0 . This happens because in cylindrical dielectric waveguides, the cutoff

frequency is given by:

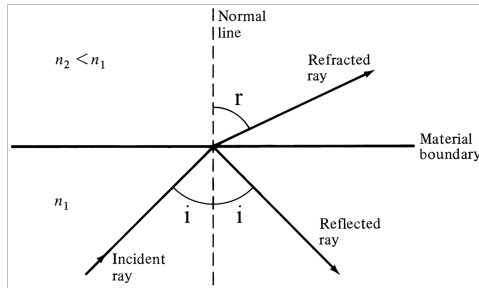
$$\omega_c = c \frac{\chi_{01}}{a_f} \Rightarrow \chi_{01} = \frac{\omega_c a_f}{c} = \frac{\omega_c a_f}{c_{wg}} n \sin \theta = \frac{2\pi a_f c_{wg}}{\lambda_c c_{wg}} NA = \frac{2\pi a_f}{\lambda_c} NA \quad (2.2)$$

where χ_{01} is the first Bessel function cutoff and λ_c is the cutoff wavelength. The $n \sin \theta$ term comes in when converting between the phase velocity of the light outside the waveguide to the phase velocity of light inside the waveguide where θ is the angle of the light entering the waveguide. Therefore, when the V-number is less than 2.4048, only the fundamental mode LP_{01} is able to propagate down the fiber.

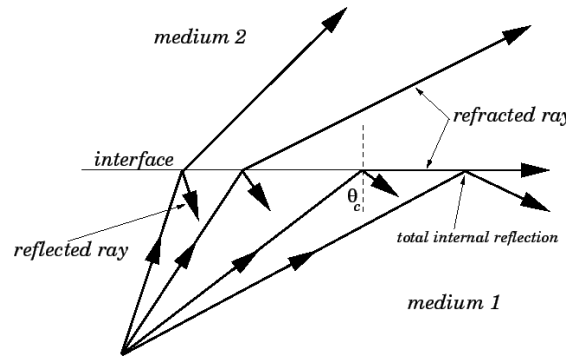
The method in which light propagates down all silica fibers is total internal reflection (TIR). TIR states that if the angle of the light propagating in a fiber with respect to the wall boundary normal is greater than some critical angle θ_c , than the light will be completely reflected back into the fiber. This angle is given by Snell's law; proposed by scientist Ibn Sahl in 984. Total internal reflection defines the critical angle as the incident angle in which the transmitted angle θ_t is 90° . At this angle, the transmitted light stays inside the waveguide by being trapped along the core/cladding boundary. Using Snell's law, we can determine what the critical angle should be for the interfaces between different medium.

$$\begin{aligned} n_1 \sin \theta_i &= n_2 \sin \theta_t \\ \sin \theta_i &= \frac{n_2}{n_1} \sin(90^\circ) \\ \theta_i = \theta_c &= \arcsin\left(\frac{n_2}{n_1}\right) \end{aligned} \quad (2.3)$$

Figure 2.2: Total internal reflection



(a) Snell's Law

(b) Multiple θ_c incident angles

As shown in figure 2.2(b), if the angle of the incoming rays are less than the critical angle, these rays will have both transmission and reflection components, losing energy outside the waveguide. Over many wavelengths, these rays will cease to propagate due to the high attenuation.

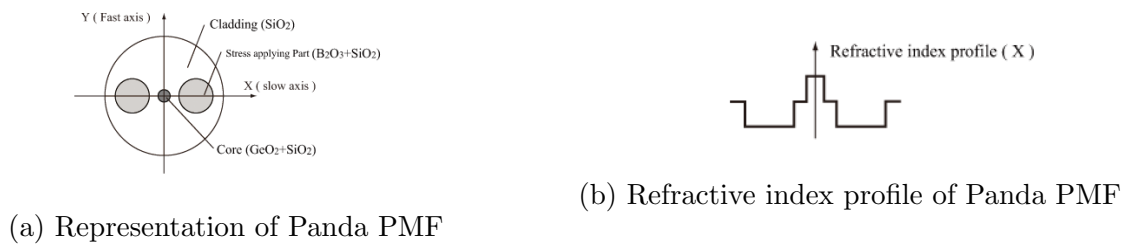
Therefore, for SMF the core's refractive index must be greater than the cladding's refractive index based on Snell's law. A usual dopant to add to silica and increase the refractive index is germanium. The SMF used for this thesis is common Corning SMF-28, which has a core radius of $4.07\mu m$, an $n_{core} = 1.45$, and an $n_{clad} = 1.444$. These parameters give a V-number of 2.17, which verifies its single mode structure at 1550 nm.

2.1.2 Panda-Style Polarization Maintaining Fiber

Polarization maintaining fiber uses all of the same principles as SMF to guide light. TIR follows from Snell's law to keep the light propagating along the fiber and is kept single-mode by virtue of its low V-number. However, the major difference between PMF and SMF is that PMF adds stress members along one axis so that different polarizations travel at different speeds. The three types of PMF used today are Panda-Style PMF, Bow-tie style PMF, and elliptical jacket PMF. Panda-Style uses circular rods as the stress member, Bow-tie style

uses trapezoidal rods to put stress on the core, and elliptical jacket style uses an elliptically shaped structure to provide different stresses on each axis. All three of these use the same basic principles to split the bounded light into its components. However, Panda-style PMF is the type of fiber used in this thesis, so that will be the focus of this section. Figure 2.3 displays the structure of a panda-style PMF.

Figure 2.3: Structure of Panda-Style PMF



As shown, the fiber core is still doped with germanium, but along one axis (z) of the fiber two boron-doped silica rods are fabricated. The boron dopant decreases the refractive index of the silica. Alongside the refractive index decrease, they also act as stress members to the core. Thus, when the stress is placed on the core, birefringence is induced due to the photo-elastic effect. The photo-elastic effect occurs when two different stresses occur in different directions, in this case along X and Y. Since there are different stresses along X and Y, each axis has a different effective refractive index. This leads to one axis becoming the "slow" axis (X) and one becoming the "fast" axis (Y). In this case, the X axis is named the slow axis because the index of refraction is higher along that axis. Since the phase velocity through a fiber is $v_p = c/n$, along the slow axis the light will travel slower. Along the Y axis, or the fast axis, the index of refraction is lower leading to a higher phase velocity.

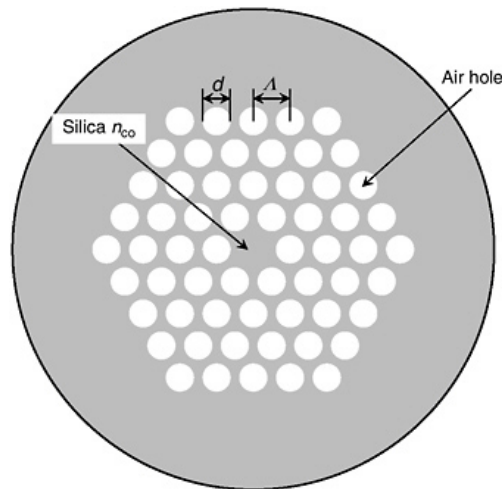
This discontinuity in the phase velocities leads to the incoming polarized light being split into its fast and slow axis components. Therefore, in this case, if light is launched along the slow axis, it will preserve the polarization to the IFPI sensor end and preserve the reflected polarization as well. How the cavity changes the polarization of the reflected light can then

be determined.

2.1.3 Photonic Crystal Fiber

The sensor tip is made from a section of Photonic Crystal Fiber (PCF). PCF, also named endlessly single-mode fiber, holey fiber or hole-assisted fiber, does not rely on doping the core to guide light. Instead, the fiber's core and cladding are made from pure silica, using a structure of air holes around the core provide the change of refractive index needed for total internal reflection [48]. An example of the end of the PCF is shown below in Figure 2.4.

Figure 2.4: Structure of a PCF showing the core and holey cladding

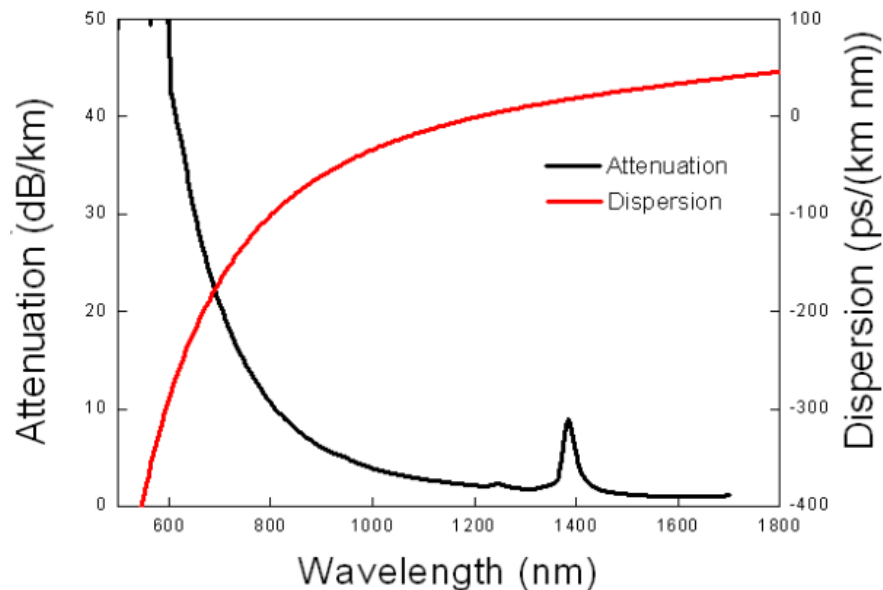


These holes provide a decrease in the effective refractive index of the area around the core. This causes the light to use the process of total internal reflection to stay in the fiber. Another interesting characteristic of PCF is that it is endlessly single mode. All doped silica fibers have what is called a cut-off wavelength λ_c , where if the incident light has a lower wavelength, the fiber is considered to be in the multimode regime. This wavelength is based off of equation (2.1), where in the V-number equation a decrease in the wavelength below

a threshold will increase the V-number over the single-mode cutoff of 2.405. In the case of PCF, however, there is no cut-off wavelength. Instead, for lower wavelengths the light is guided in less of the holey region and, therefore, more to the core of the fiber reducing the mode-field diameter (MFD).

The practical limit on the bandwidth is the amount of loss that occurs in guiding particular wavelengths. Looking at Figure 2.5 which contains the attenuation and dispersion curves for the PCF fiber used (NKT Photonics ESM-12B), both of these factors play a role in the range of wavelengths supported.

Figure 2.5: Typical attenuation and dispersion curves for PCF



Based on these factors, PCF can sustain a wide wavelength range if you are able to compensate for the dispersion effects or the attenuation.

In the case of this thesis, however, the holey structure is only used to make an IFPI cavity. After the cavity is etched out, only the core is left as a suspended microfiber with a cladding of air. This structure will not be single-moded, but the number of modes must be restricted

so that the resulting spectrum is clean. For single-mode operation, we can use equation 2.1 and substitute in 2.405 for V to find the cutoff radius. Since the bandwidth in this work has $1.55 \mu\text{m}$ at about the center, it is used as λ . Based on previous values, $n_1 = n_{\text{silica}} = 1.444$ and $n_2 = n_{\text{air}} = 1$.

$$\begin{aligned}
 V &> \frac{2\pi a}{\lambda} \sqrt{n_1^2 - n_2^2} \\
 2.4048 &> \frac{2\pi a}{1.55 \mu\text{m}} \sqrt{1.444^2 - 1^2} \\
 a &< .57 \mu\text{m}
 \end{aligned} \tag{2.4}$$

Therefore, to keep the microfiber completely the single-mode regime, the core radius must be less than $.6 \mu\text{m}$. When this occurs, only the fundamental mode is able to propagate in the core IFPI cavity. Since more than one mode will be propagating in the fiber, we can use

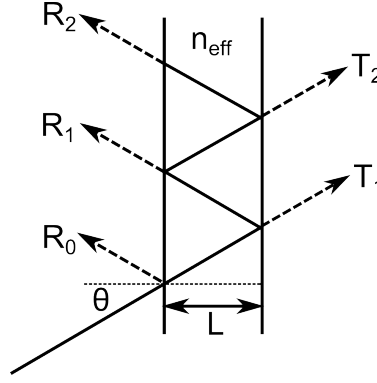
$$N = \frac{V^2}{2} \tag{2.5}$$

where N is the number of modes that the step-index structure supports.

2.2 IFPI Cavities

IFPI cavities are very simple in their construction and are based on a Fabry-Perot etalon structure. The IFPI structure is similar to the Fabry-Perot etalon in Figure 2.6.

Figure 2.6: Fabry-Perot etalon structure



This drawing places two partially-reflecting mirrors a distance L from each other. The light is injected into the cavity at an angle θ and with each partial reflection, a portion of the light is transmitted and the other portion reflected. The subsequent transmissions or reflections that escape the cavity will constructively and destructively interfere based on wavelength.

In the case of the interferometer, θ is set to 0 since light is injected into the cavity orthogonally. Also, since the sensor presented relies on reflected light, the transmitted light will be lost to free space. With this setup the optical path distance (OPD), defined as the distance the light travels between the partially-reflecting mirrors, is given as:

$$\begin{aligned} OPD &= 2n_{eff}L \cos \theta \\ &= 2n_{eff}L \end{aligned} \tag{2.6}$$

In this equation, the n_{eff} is the effective refractive index inside the cavity. Therefore, there is a phase delay between two successive waves. This phase delay is given as

$$\delta = \frac{2\pi OPD}{\lambda_0} = \frac{4\pi n_{eff}L}{\lambda_0} \tag{2.7}$$

Because there is phase delay between the two waves, there is a point at which they are in

phase and constructively interfere. With wavelengths of constructive interference, there is maximum transmission on either side of the cavity. This occurs when $\sin(\delta/2) = 0$, or when $\delta/2 = m\pi$ where m is an integer, thus the maximum happens whenever

$$\frac{4\pi n_{eff}L}{\lambda_0} = 2m\pi \quad (2.8)$$

For this relationship to be true, $L = m\lambda/2n_{eff}$. The wavelength and frequency peaks can be found as

$$\begin{aligned} \lambda_m &= \frac{2n_{eff}L}{m} \\ \nu_m &= \frac{mc}{2n_{eff}L} \end{aligned} \quad (2.9)$$

Knowing the wavelength peaks, it follows that the free spectral range (FSR) can be calculated. The free spectral range is defined as the wavelength difference between neighboring peaks. The FSR is, therefore,

$$\begin{aligned} \Delta\lambda &= \frac{\lambda_0^2}{2n_{eff}L} \\ \Delta\nu &= \frac{c}{2n_{eff}L} \end{aligned} \quad (2.10)$$

in terms of wavelength or frequency respectively, however, only the wavelength domain will be used due to other measurements being taken in wavelength units instead of frequency units. Using the FSR, we can calculate the number peaks over a certain bandwidth which is useful in giving a rough estimate of the cavity length given a spectrum.

$$N = \frac{\Delta\Lambda}{\Delta\lambda} \quad (2.11)$$

where $\Delta\Lambda$ is the input spectrum bandwidth. The finesse can be found by

$$\mathcal{F} = \frac{\Delta\lambda}{\delta\lambda} \quad (2.12)$$

where $\delta\lambda$ is the full-width half-maximum (FWHM) of the resulting fringes. Finesse is a measure of the sharpness of the fringe pattern's peaks. It depends on the reflectivity of the mirrors creating the cavity. Low reflectivity mirrors create low-finesse cavities which translate to broader fringes. Alternatively, if high-reflectivity mirrors are used, high-finesse cavities are achieved with sharper transmission peaks.

These cavities are also very susceptible to changes in length, ambient temperature, and refractive index. Since these cavities rely on constructive and destructive interference for their fringe pattern, all three of these effects will change the phase of the light and shift the spectrum. For changes in length, which would be due to stretching and compressing effects [49],

$$\Delta\delta = \frac{4\pi n_{eff}\Delta L}{\lambda} \quad (2.13)$$

where ΔL is the change in cavity length. The refractive index of silica glass depends on the temperature of its environment. When the refractive index changes there is a phase shift in the cavity given by [49]

$$\Delta\delta = k_0 L \left(\frac{dn_{eff}}{dT} + \frac{n_{eff}}{L} \frac{dL}{dT} \right) \Delta T \quad (2.14)$$

where k_0 is the wave number in a vacuum ($k_0 = 2\pi/\lambda$), $\frac{dn_{eff}}{dT}$ is the thermo-optic coefficient, and $\frac{dL}{dT}$ is the thermal expansion coefficient of the PCF sensing tip. When there is a phase shift produced, equations (2.7) and (2.9) show that the corresponding wavelength and frequency peaks would be linearly shifted as well.

Characterizing the effects of ambient refractive index on the microfiber tip is more involved. To characterize them completely, the propagation constant must be found as the surrounding

index changes. The weakly guiding assumption can be used in this case [50].

To start, we know that the propagation constant must be between

$$n_{core}k_0 \leq \beta \leq n_{clad}k_0 \quad (2.15)$$

the parameters u and w can then be defined such that

$$\begin{aligned} u &= a\sqrt{k_0^2 n_{core}^2 - \beta^2} \\ w &= a\sqrt{\beta^2 - k_0^2 n_{clad}^2} \end{aligned} \quad (2.16)$$

These two expressions, when combined, create the V-number equation

$$\begin{aligned} V^2 &= u^2 + w^2 \\ V &= ak_0\sqrt{n_{core}^2 - n_{clad}^2} \end{aligned} \quad (2.17)$$

The weakly guiding assumption states that

$$\Delta = \frac{n_{core} - n_{clad}}{n_{clad}} \ll 1 \quad (2.18)$$

From Eq. (2.16)-(2.18), the normalized propagation constant can be obtained, which is

$$b = 1 - \frac{u^2}{v^2} = \frac{\beta^2/k_0^2 - n_{clad}^2}{n_{core}^2 - n_{clad}^2} \quad (2.19)$$

which, taking into account the weakly guiding assumption, reduces to

$$b = \frac{\beta/k_0 - n_{clad}}{n_{core} - n_{clad}} \quad (2.20)$$

Rearranging this equation with the weakly guiding assumption gives

$$\beta = nk(b\Delta + 1) \quad (2.21)$$

Now, since this microfiber is still in the multimode regime, the cutoff of the ν th mode can be given as

$$u_c = \sqrt{2\nu} \quad (2.22)$$

Then, u in equation (2.19) can be substituted by u_c and reduced to

$$b = 1 - \frac{u_c^2}{v^2} = 1 - \frac{\nu}{N} = 1 - \frac{2\nu}{V^2} \quad (2.23)$$

For this case, the fundamental mode will be the main mode in the cavity, so $\nu = 1$. Equation (2.23) can then be substituted into equation (2.21) to get the propagation constant

$$\beta = n_{clad}k_0 \left(1 + \Delta \left(1 - \frac{2}{V^2} \right) \right) \quad (2.24)$$

Since the propagation constant $\beta = n_{eff}k_0$, equation (2.24) becomes

$$n_{eff} = n_{clad} \left(1 + \Delta \left(1 - \frac{2}{V^2} \right) \right) \quad (2.25)$$

With the effective index, the cavity resonance wavelength shifts can be found.

$$\lambda_{shift} = 2n_{eff2}L - 2n_{eff1}L \quad (2.26)$$

Based on these equations, the length and effective index of the cavity plays a major role in determining the fringe pattern and finesse of the reflection spectrum. In the case of this sensor, the splice of the PCF and SMF/PMF makes up the first partially-reflecting mirror

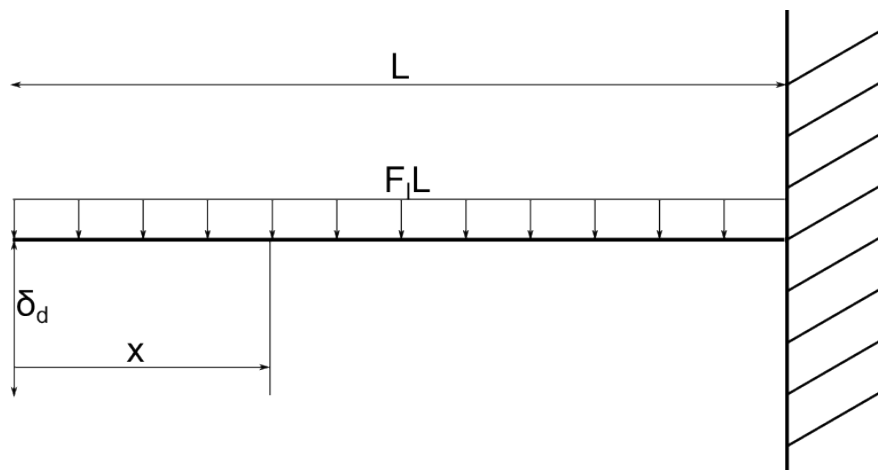
and the cleave of the PCF on the other side makes up the second, thus these two mirrors form the cavity and the above equations define its properties.

When the PCF structure is etched out, the resulting cavity can be represented as a cantilever beam.

2.3 Cantilever Beams

As a microfiber core supported only on one side, the internal structure can be modeled mechanically as a cantilever beam when subjected to a tangential acceleration. Since the entire core is feeling the force of this acceleration, we can assume that the cantilever beam is acting as as if it has a uniformly distributed load [44].

Figure 2.7: Uniformly distributed load cantilever beam



In Figure 2.7, L is the total length of the beam, x is the distance from the tip, and F_l is the force per unit length on the beam. The force can first be broken down by using Newton's second law

$$F_l = ma = (A\rho dl)a \quad (2.27)$$

where A is the cross-sectional area of the beam, ρ is the mass density, a is the acceleration, and dl is per unit length. With this configuration, the elastic deflection of the cantilever beam with this force is given by

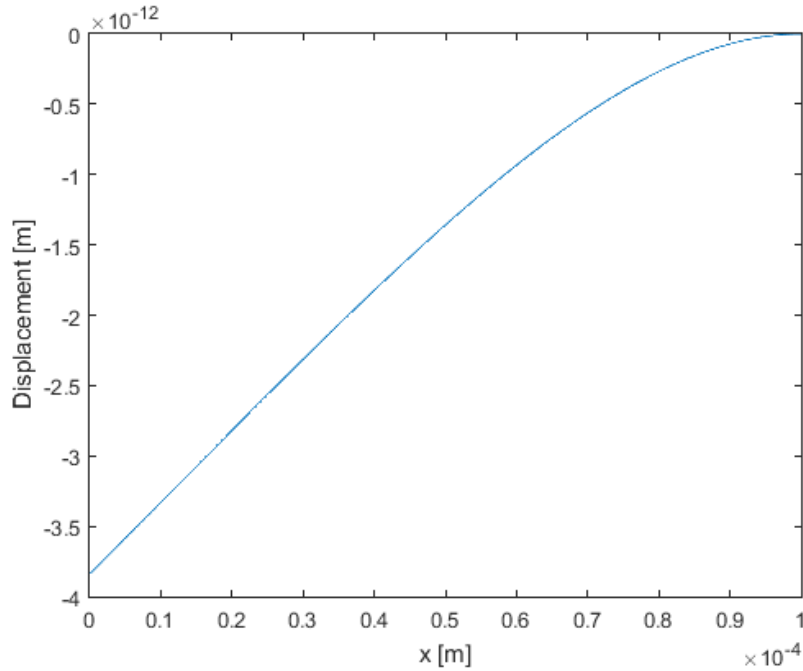
$$\begin{aligned} \delta_d(x) &= \frac{F_l}{24EI}(x^4 - 4L^3x + 3L^4) \\ \delta_d(0) &= \frac{F_l L^4}{8EI} = \frac{A\rho L^4 a}{8EI} \end{aligned} \quad (2.28)$$

where E is Young's modulus and I is the moment of inertia of the beam at the fixed end. Since the beam is a cylinder,

$$I = \frac{\pi a_f^4}{4} \quad (2.29)$$

where a_f is the radius of the fiber core. PCF is made from pure silica so the values of fused silica can be used for the material characteristics: $\rho = 2.203 \text{ g/cm}^3$ and $E = 71.7 \text{ GPa}$. For a representative values of $a = 10 \text{ m/s}^2$, $a_f = 2 \text{ }\mu\text{m}$, and $L = 100 \text{ }\mu\text{m}$, the core would bend as shown in figure 2.8.

Figure 2.8: Displacement of cantilever beam under load



This plot shows how the cantilever beam will be affected by the acceleration. With a length of $100 \mu\text{m}$ the beam will have a maximum displacement of around 3.8 pm .

Based on the previous values, the resonance frequency of this structure can be found. The resonance frequency specifies the maximum frequency that can be measured with the beam [44].

$$f_{res} = \frac{1}{2\pi} \sqrt{\frac{8EI}{\rho AL^4}} = \frac{1}{2\pi} \sqrt{\frac{2Ea_f^2}{\rho L^4}} \quad (2.30)$$

With the representative values, the resonant frequency of the beam would be 257 kHz . This means the sensor is best used below the resonant frequency. It can be noted that this resonant frequency has the relationship $f_{res} \sim 1/L^2$, which means that the length of the cantilever beam has a large impact on the maximum measured frequency.

Figure 2.8 also shows that the radius of curvature is maximum around the fixed end of the core. To find the radius of curvature, the bending moment of the beam is needed. The bending moment of a uniformly loaded cantilever beam is given as

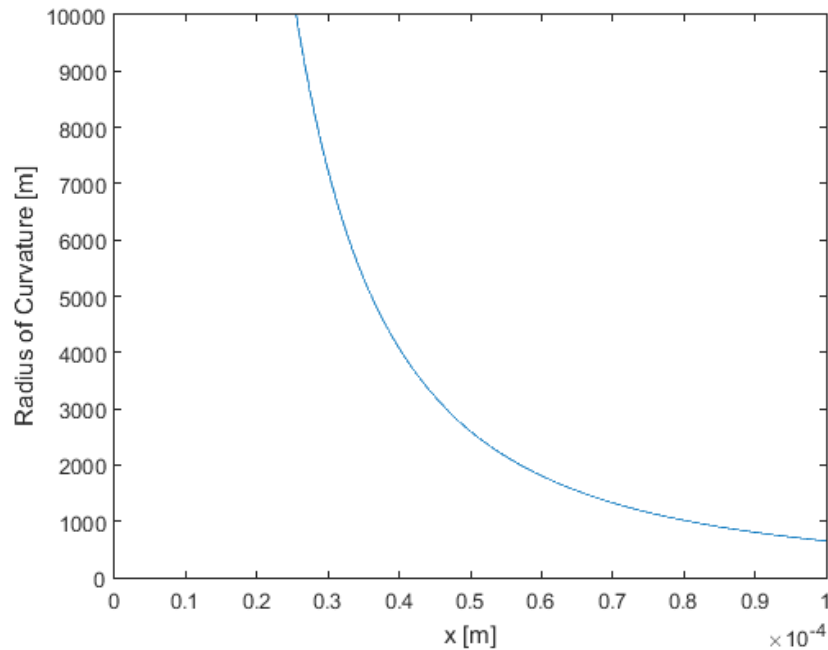
$$\begin{aligned}M(x) &= \frac{F_t x^2}{2} \\M(L) &= \frac{F_t L^2}{2}\end{aligned}\tag{2.31}$$

Based on this equation, the bending moment of the beam is maximum around the fixed end. Using equations 2.12, the radius of curvature can be found by

$$\begin{aligned}\frac{1}{R(x)} &= \frac{M(x)}{EI} \\R(x) &= \frac{EI}{M(x)} = 2 \frac{EI}{F_t x^2}\end{aligned}\tag{2.32}$$

Using the same values as in figure 2.8, the radius of curvature is shown in Figure 2.9.

Figure 2.9: Radius of curvature for a cantilever beam under load



The radius of curvature of the suspended core with the previous values is at minimum 651 m. This means that macrobending is the main contributor of bending since microbending occurs when the bending radius is very small.

2.4 Macrobending

The distinction between macrobending and microbending is the differences in the radius of curvature. Corning makes this distinction by specifying the radius of curvature cutoff between the two at around 1 mm [51]. Therefore, since the radius of curvature of our test case is sufficiently over that cutoff the fiber is experiencing macrobending.

Macrobending is perceived by the fiber as a tilt in the refractive index. When a fiber experiences macrobending, one side of the fiber compresses causing an increase in the effective

refractive index on that side, and the other side stretches causing a decrease in the effective refractive index.

However, with the radius of curvature this large there is only a small change in the refractive index. The refractive index changes as

$$n(r) = n_0^2 + \frac{2n_0^2 r}{R} \quad (2.33)$$

This means that at $r = \pm a_f$, the index will change $\pm 2.21 \times 10^{-9}$ RIU. This is much too low to be picked up by this sensor; for tangential acceleration, there is an undiscovered factor that causes the wavelength shift.

Chapter 3

Sensor Structure

3.1 Fabrication

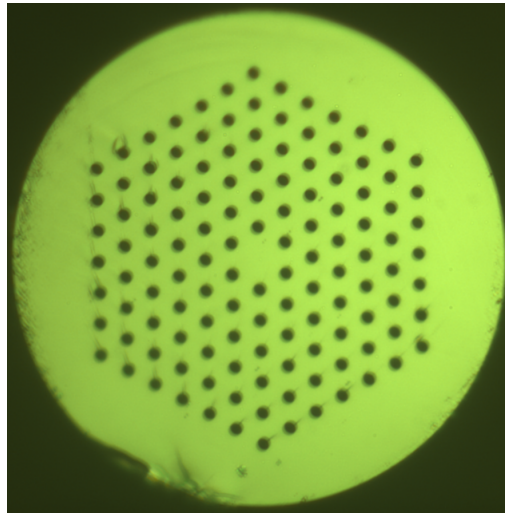
The fabrication process follows closely to what was previously done by R. Wang [35–37]. However, where he only used SMF both SMF and PMF are used in this work as lead-in fibers. Using the PMF instead of SMF does not add any complications to the procedure.

3.1.1 Pre-etching Fiber Parameters

The pre-etching fiber parameters were replicated from the previous work from R. Wang and through trial and error. This section of the process will focus on the procedure before etching.

The PCF that was used for this sensor was the ESM-12B from ThorLabs. The end of this fiber before etching is shown in figure 3.1 below.

Figure 3.1: ESM-12B PCF end



The specifications of this fiber are a cladding size of $125\ \mu\text{m}$ and a core size of $12\ \mu\text{m}$. Approximate dimensions from ThorLabs' fiber unit include an air hole diameter of approximately $3.5\ \mu\text{m}$ and a hole spacing of approximately $8\ \mu\text{m}$. These contrast with R. Wang's values of a $7\ \mu\text{m}$ core diameter, $2.57\ \mu\text{m}$ air hole diameter, and $5.12\ \mu\text{m}$ air hole spacing. These differences do not affect the pre-etching part of the procedure, but will in the etching process.

The SMF that was chosen as the lead-in fiber is the SMF-28 from Corning. The SMF-28 has a core diameter of $8.2\ \mu\text{m}$ and a cladding diameter of $125\ \mu\text{m}$. The light is contained by total internal reflection with a numerical aperture of 0.14. This makes the V-number 2.3, confirming its single-mode status at $1550\ \text{nm}$. The PMF used was a patchcord that was cut in half to turn both ends into fiber pigtailed. This patchcord contained the PM1550-XP from ThorLabs. This fiber has the wavelength range of $1440\ \text{nm}$ to $1625\ \text{nm}$, a core diameter of $8.5\ \mu\text{m}$, and a cladding diameter of $125\ \mu\text{m}$. Both of these fibers are suited for their respective tasks.

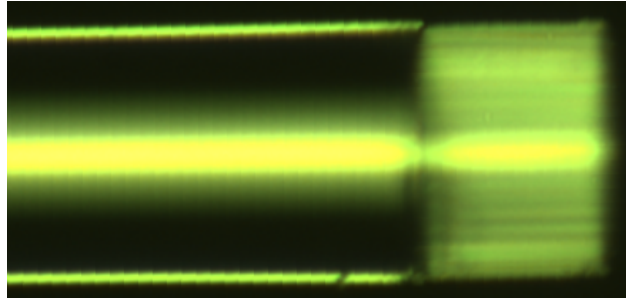
With the ESM-12B the splicing procedure is the same using either SMF or PCF. The first step is to splice the PCF and the lead-in fiber together. The Fukijura FSM-45PM precision

splicer was used for this because of its flexibility and range of tuning parameters. The splicer is then set to SMF-SMF splicing mode and modified to splice the SMF/PMF to PCF. The alignment setting is changed from core to cladding since both types of fibers use a $125\ \mu\text{m}$ diameter cladding, but have different core diameters. The splicing power is reduced from 20 bits to -30 bits and the duration is changed from 800 ms to 300 ms. The final change is that the overlap between the fibers is decreased from $15\ \mu\text{m}$ to $5\ \mu\text{m}$. Reducing these parameters is vital so air holes in the PCF do not collapse during splicing and a bubble does not form at the splicing point. If the air holes collapsed or a bubble formed at this stage, the cavity would not be uniform during the etching process and could cause irregularities. The result is a splice between the two fibers, however, the splice is very weak and prone to breaking. Great care must be taken with the following step to insure a clean cleave.

The next step in the process is to cleave the fiber. The Fukijura CT-32 precision cleaver was used first, but was found to not provide a clean enough cleave for this splice and caused the fiber to break at the splicing point instead of the cleaving point more often than not. Instead, the cleave must be done manually under a microscope. The cleaver found to work best for this application is the Lynx by Fiberoptic Instrument Sales. With this cleaver under the microscope, the blade is lined up to the cavity length specified and cleaved. Initially, there were problems with using this method since the PCF was too long to be taut against the blade. This caused the fiber to break at the splicing point every time it was cleaved. To remedy this, the PCF was taped to a fiber spool and wound until taut. This new method produces clean cleaves approximately 25% of the time increased from approximately 10% with the precision cleaver.

The length of the cavity, and subsequently the cantilever core, is a major consideration of the sensor. I have found through testing that $100\ \mu\text{m}$ is a reasonable length and is shown in Figure 3.2.

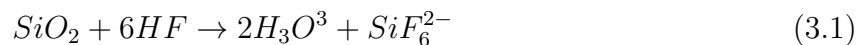
Figure 3.2: ESM-12B PCF side view



The reasoning behind why $100\ \mu\text{m}$ is a good length will be explained and shown in the following sections. However, after these two steps are successfully completed the etching process begins.

3.1.2 Etching Considerations

The procedure for etching is straightforward, but the etching time varies depending on the fiber used, the structure desired, and the etchant contamination level. For etching this structure, the end of the fiber is dipped into hydrofluoric acid. Hydrofluoric acid is pre-combined with water at a ratio of 1:1 to prevent rapid evaporation. When this substance comes into contact with the silica in the PCF, the chemical reaction that takes place is given by [52]



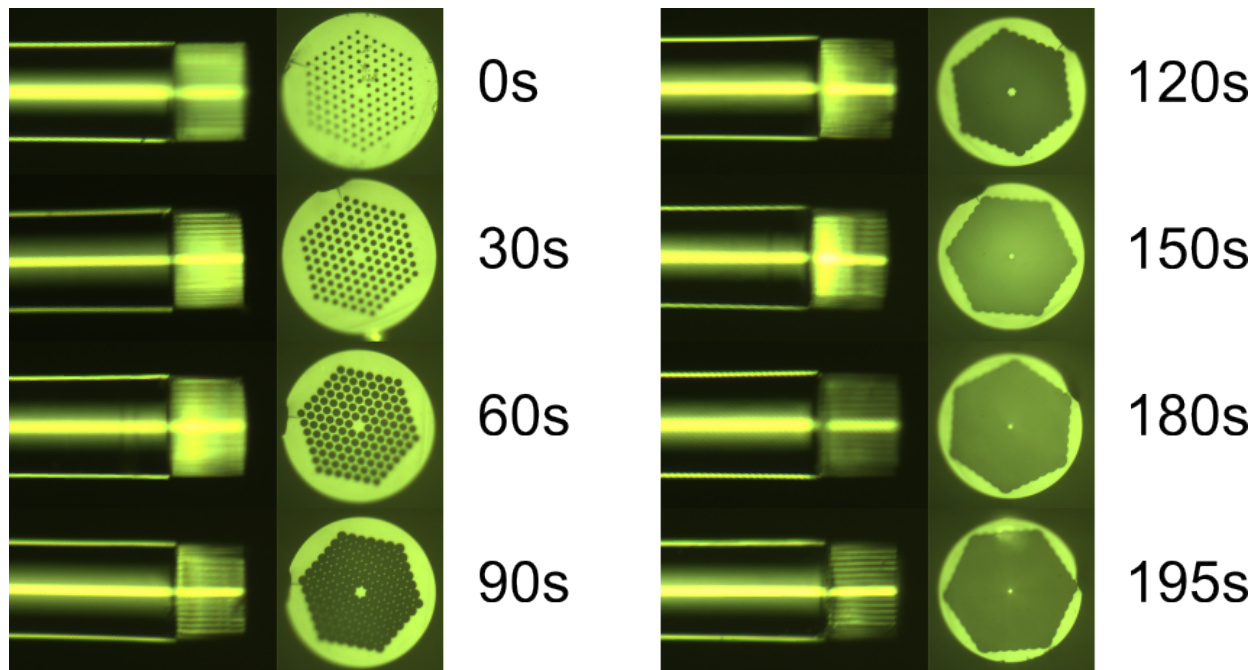
So, based on this equation, the HF reacts with the SiO_2 to produce H_3O^3 and SiF_6^{2-} , contaminants which are harmful to breathe and slow the etching process. Over time, this occurs because more HF is used up in the etching so there is a lower concentration of molecules to react with the silica. To make sure etching times are consistent, .5 mL of the

HF solution is used for two sensors; any more and the etching time is further decreased.

When the fibers are placed into the *HF* solution, the air holes of the PCF are filled and the *HF* erodes the structure and enlarges the holes. This initial erosion occurs at the same rate for both lead-in fibers. However, they diverge slightly when the PCF erodes enough that the solution reaches the lead-in fiber. Borosilicate erodes faster than the silica, so when the borosilicate stress rods in the PMF are exposed, they are eaten through faster than the silica.

With either lead-in fiber, the etching looks the same under a microscope. To visualize how this process occurs over time, an etching was done with an SMF at 30 second intervals. With each etch, the fiber was cleaned, its spectrum was taken, and pictures were taken of its side and end face. The photos are shown in figure 3.3 below.

Figure 3.3: SMF etching progression



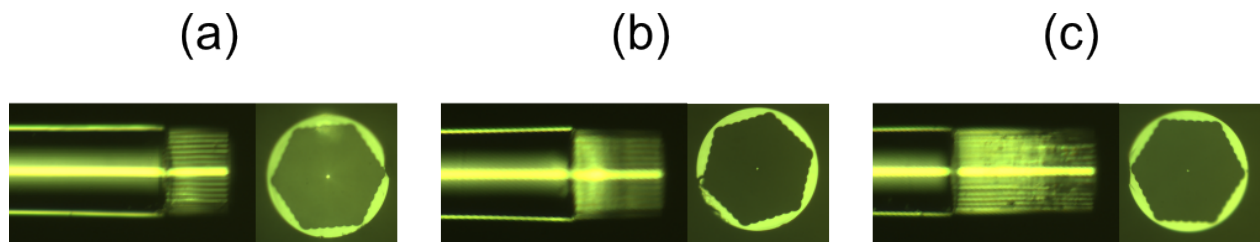
As shown by this progression, the internal structure is etched out as the core diameter

decreases. At around 90 seconds of etching, the internal structure is almost completely etched out. After this point, the HF solution etches the suspended core from all sides along its length down to $\sim 3\ \mu\text{m}$ in diameter after 195 seconds of etching time. In the previous work by R. Wang, the etching time was much less at 120 seconds. This is due to the fact that his core diameter started at $7\ \mu\text{m}$ instead of $12\ \mu\text{m}$ so it took much less time to etch down to $3\ \mu\text{m}$.

When looking at the side profile case, it is hard to discern the depth at which the etching has eaten through in the 30 second intervals. However, comparing zero seconds of etching to 180 or 190 seconds of etching a clear distinction can be made. At zero seconds the PCF looks filled in and it is hard to make out individual air holes viewing from the side. Contrasting that to 195 seconds of etching, the PCF cavity is darker signifying empty space, but lines can also be seen horizontally. These lines are due to the ribbed structure left on the sides of the PCF after the internal structure has been etched out.

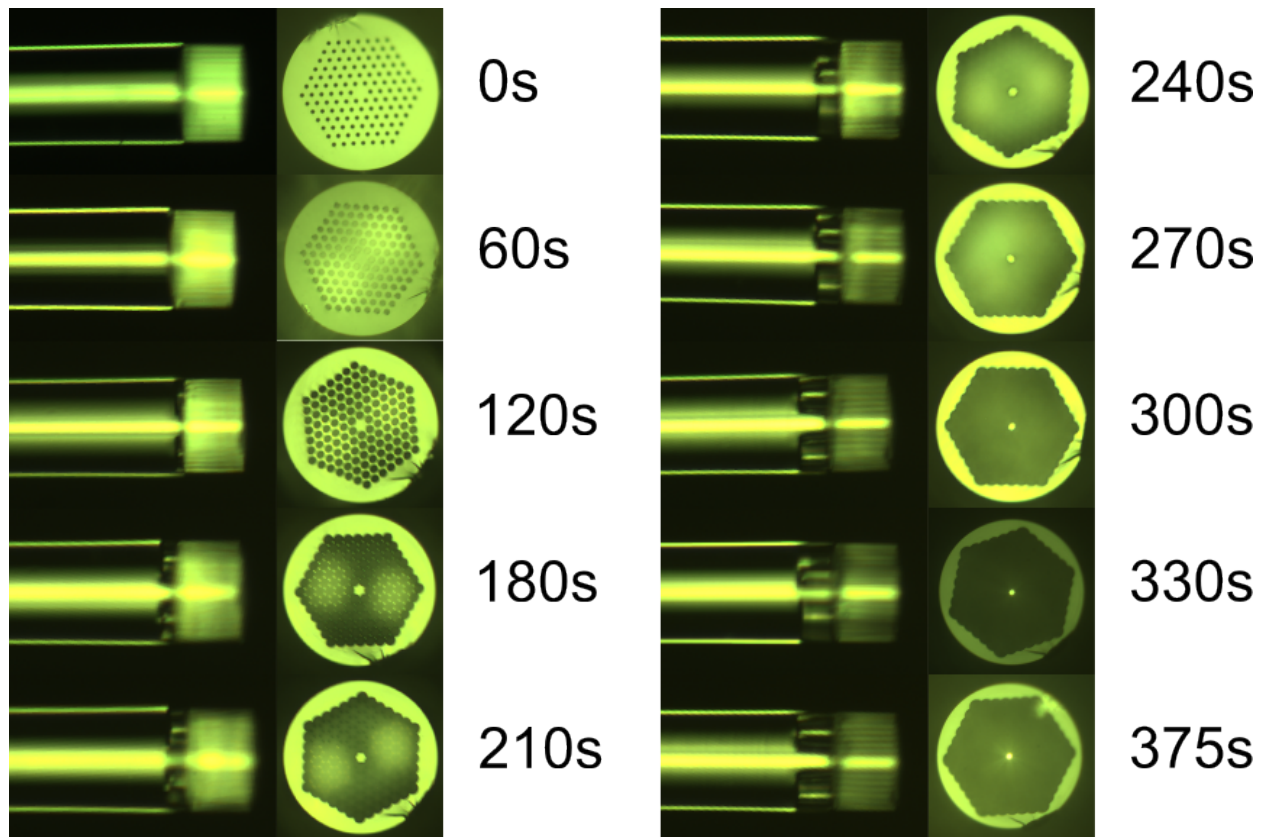
Through testing various cavity lengths in the SMF lead-in case, it was found that the length of the PCF spliced to the fiber has a large impact on the resulting spectrum's fringe depths. This is due to the difficulty of the HF in traversing up the air holes to the splicing point when dipped into the etchant. This process was tested for lengths of $150\ \mu\text{m}$ and $200\ \mu\text{m}$ to determine that this was the cause. The cases for $150\ \mu\text{m}$ and $200\ \mu\text{m}$ cavity lengths at 195 seconds of etching is shown below in Figure 3.4.

Figure 3.4: SMF etching after 195 s for (a) $100\ \mu\text{m}$, (b) $150\ \mu\text{m}$, and (c) $200\ \mu\text{m}$ length cavities



As shown in Figure 3.4, the etching does not reach the lead-in fiber after the etching is complete. If the etching time is increased further, the core will be etched through completely, which is undesired. The PMF case is shown in figure 3.5.

Figure 3.5: PMF etching progression



Between the original batch of SMF and when the first batch of PMF sensors were produced, the *HF* solution was contaminated leading to higher etching times. The contamination only increases the etching time of the cavity without any negative repercussions to the performance of the sensor. When etching another SMF sensor after the solution was contaminated, the etching time increased from 195 seconds to 370 seconds, comparable with the PMF case. In each time step up until around 270 seconds, the borosilicate rods can be seen as they are

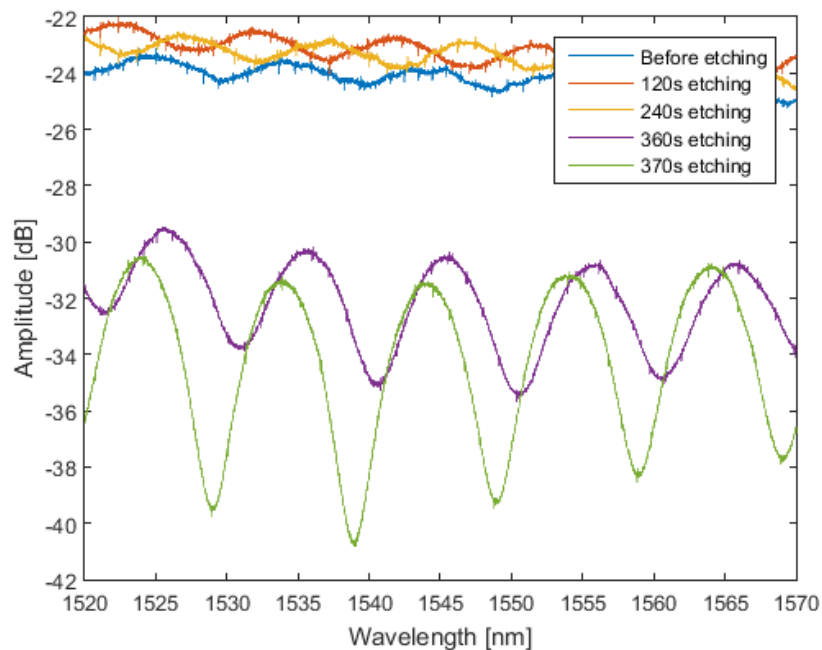
etched out. They do not effect the cavity length at all and they are shallow enough that they do not have a significant effect on the polarization maintaining ability of the fiber.

3.2 IFPI Performance

3.2.1 SMF Case

The progression of the spectrum with respect to time is gradual up until the air holes are completely etched out, but becomes dramatic the smaller the core becomes. This is shown in figure below with the etching progression of an SMF.

Figure 3.6: SMF etching progression



For the first 240 seconds, of etching the IFPI spectrum is at a fairly constant level with some wavelength shifting. Looking at figure 3.5, 240 seconds is about the time it takes for the

internal structure to be completely etched out. After the cladding is etched, the fiber diameter plays the major factor in the fringe pattern. This occurs due to multimode interference in the IFPI section. After etching 240 seconds, the fiber diameter is approximately $7\ \mu\text{m}$. Using equation 2.1, the V-number would be 14.8. This means that the fiber is definitely not single mode and there are approximately 110 modes propagating in the short section of fiber. These modes interfere with each other and cause a shallow fringe pattern. As the core diameter is etched smaller, the fringe pattern due to less modal interference. Finally, at 370 seconds of etching, the core diameter reaches approximately $4\ \mu\text{m}$ and supports about 35 modes. Further etching could be done to potentially increase the fringe pattern, however, there is an increased risk of etching the core too much.

Using the 370 seconds etch as the final result, the FSR, finesse, and true cavity length can be discerned. For this sensor, the peaks are calculated to be exactly 10 nm apart when looking between the 1543 nm and 1553 nm peaks. Therefore, from this FSR value, the true cavity length can be calculated from equation (2.7) after finding the effective index through equation (2.25)

$$\begin{aligned}\Delta\lambda &= \frac{\lambda_0^2}{2n_{eff}L} \\ 10\ \text{nm} &= \frac{(1548\ \text{nm})^2}{2(1.4315)L} \\ L &= 83.7\ \mu\text{m}\end{aligned}\tag{3.2}$$

The finesse, defined by equation 2.9, can be found with the FSR and FWHM. With the final fringe pattern, the calculated FWHM is 6.2 nm which gives a finesse of

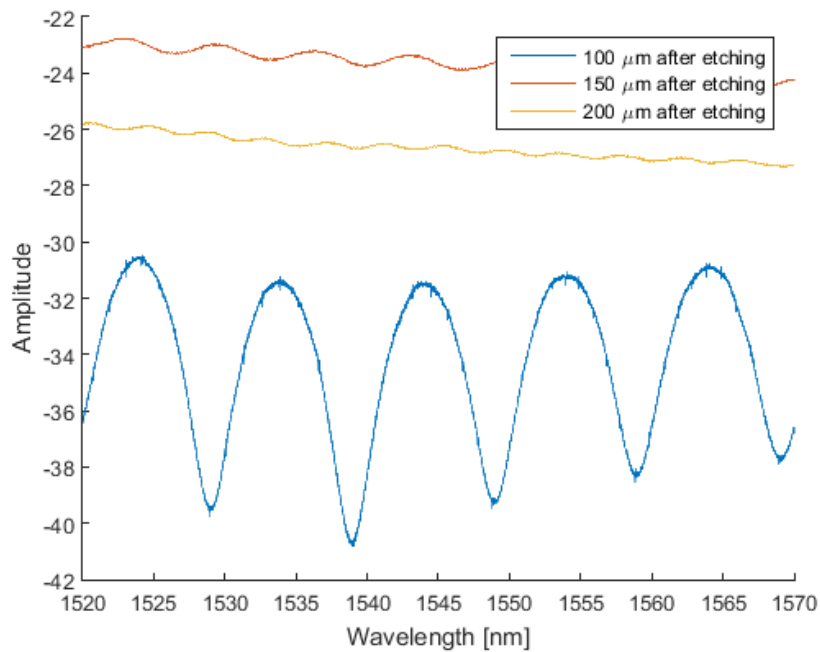
$$\mathcal{F} = \frac{\Delta\lambda}{\delta\lambda} = \frac{10\ \text{nm}}{6.2\ \text{nm}} = 1.6\tag{3.3}$$

This cavity is considered a low-finesse fabry-perot resonator.

A large impact on the finesse and the fringe pattern of this sensor is its length. At $100\ \mu\text{m}$

the calculated number of peaks from equation 2.8 is 5 with the CTS bandwidth $\Delta\Lambda = 50 \mu\text{m}$. This number increases to 7.5 with a $150 \mu\text{m}$ cavity and 10 with a $200 \mu\text{m}$ cavity. After etching the core to approximately $4 \mu\text{m}$ in diameter in each case, the resulting spectrum are shown in figure 3.7.

Figure 3.7: Spectrum with different cavity lengths



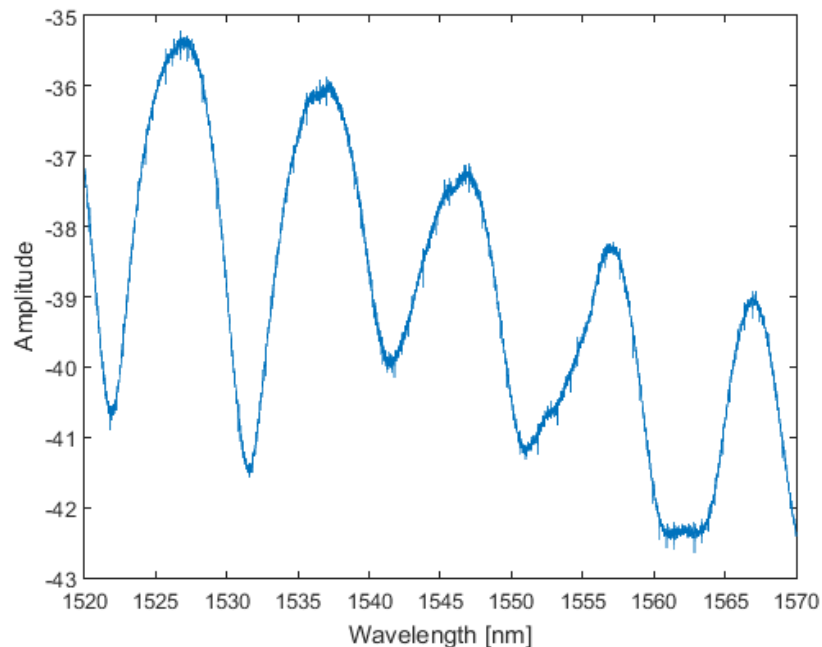
Even with the same microfiber tip diameter the different cavity lengths create very different spectrum. As predicted, the $150 \mu\text{m}$ cavity has 7.5 fringe peaks and the $200 \mu\text{m}$ cavity has 10 peaks. Since the etching can not penetrate deeply into the longer cavities, the fiber core is etched at different lengths. The spectra are so different due to multimode interference and tapering of the microfiber core in the $150 \mu\text{m}$ and $200 \mu\text{m}$ cases. For the longer cases, a fiber taper develops due to the different etching rates of the core fiber. With this taper, reflections will be made off of the end cleave as well as the sides of the taper. This makes an FP cavity with has multiple lengths and causes the spectrum to be much less defined.

With these multiple lengths, there are also many more modes that are able to propagate. When the fiber diameter increases along the taper more modes are able to propagate in that section. Both of these effects cause a spectrum which have a finesse of zero since neither of them have a FWHM, which needs a depth of 3-dB to measure. Therefore, $100\ \mu\text{m}$ is chosen as a good cavity length for this sensor.

3.2.2 PMF Case

The case of the PMF is very close to that of the SMF. With the cleave length already well defined, it was replicated again with a different lead-in fiber. The resulting spectrum after etching the core down to around $4\ \mu\text{m}$ is shown below.

Figure 3.8: PMF spectrum after etching



This spectrum is somewhat different than the case with the SMF. In this case, the spectrum

is tilted and deformed at higher wavelengths. This is due to the etching process with the borosilicate rods. In that etching process, along the slow axis of the fiber the rods are etched out quicker than the silica. Therefore, when the etchant comes into contact with the rods, that axis is etched slower due to the influx of contamination. This happens quite early in the etching process. Along that axis the fiber is etched slower and the air-hole structure stays in place longer. This causes an imbalance in the cavity since the cylindrical symmetry of the fiber is affected. The tilted spectrum does not effect the measurements made since the PMF was only used in testing tangential acceleration and, therefore, at quadrature.

As like with SMF, the cavity length and finesse of the sensor can be found. The FSR was found based on the first two peaks. They give us that

$$\begin{aligned}\Delta\lambda &= \frac{\lambda_0^2}{2n_{eff}L} \\ 10.1 \text{ nm} &= \frac{(1530 \text{ nm})^2}{2(1.4315)L} \\ L &= 81 \mu\text{m}\end{aligned}\tag{3.4}$$

which is very close to what the cavity length was for the SMF case. The calculated FWHM of this pattern is 7.2 nm which gives a finesse of

$$\mathcal{F} = \frac{\Delta\lambda}{\delta\lambda} = \frac{10.1 \text{ nm}}{7.2 \text{ nm}} = 1.4\tag{3.5}$$

With this finesse, this cavity would also be considered a low-finesse IFPI.

Chapter 4

Testing

This chapter outlines the three tests performed using an SMF as the lead-in fiber. Using a PMF lead-in would not improve on the performance in any of these test cases. Where the PMF lead-in excels is in the case where tangential acceleration with direction needs to be found. This is left to future work in Chapter 5.

4.1 Temperature Testing

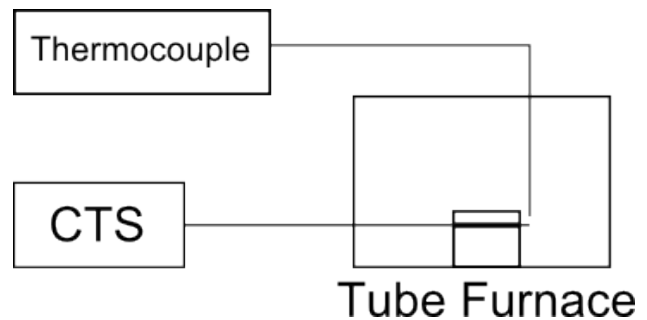
A temperature dependence curve is needed as a baseline for all other measurements. Because the suspended core is made from silica, there will be some temperature shifts of the spectrum as discussed in chapter 2.2.

To measure this shift, a tube furnace was used due to its high heat tolerance; specifically, the Thermolyne 47900. This tube furnace is unable to be programmed so the temperature must be set manually. Furthermore, due to the shape of the furnace and placement of the heating coils, the inside is heated asymmetrically. This problem can be solved by using a thermocouple at the sensor tip to find the actual temperature of the area. Figure 4.1 shows the test being run (a) and a diagram of the test setup (b).

Figure 4.1: Temperature testing setup



(a) Furnace during testing



(b) Temperature furnace test setup

As shown in (a), the fiber with the sensor at its tip is placed through the front of the furnace, while the thermocouple is placed through the top. This ensures that both points meet like in (b). The fiber inside the furnace is placed between two aluminum blocks to prevent the fiber from moving during the testing and to place the fragile fiber tip into the furnace easier. The thermocouple that was used has an LCD display with the temperature so that accurate frames could be taken from the CTS at precise temperature points. The CTS that was used is the sm125 from Micron Optics, the same one used with the IFPI performance testing.

To test this setup, the temperature in the furnace was slowly raised and measurements were taken from the starting temperature of around 25 °C to 300 °C. The temperature was kept at 300 °C to ensure that the suspended core would not bend; if the core gets too hot, it would bend and irreparably damage the sensor. The results from this testing are shown below in Figure 4.2.

Figure 4.2: Temperature testing results

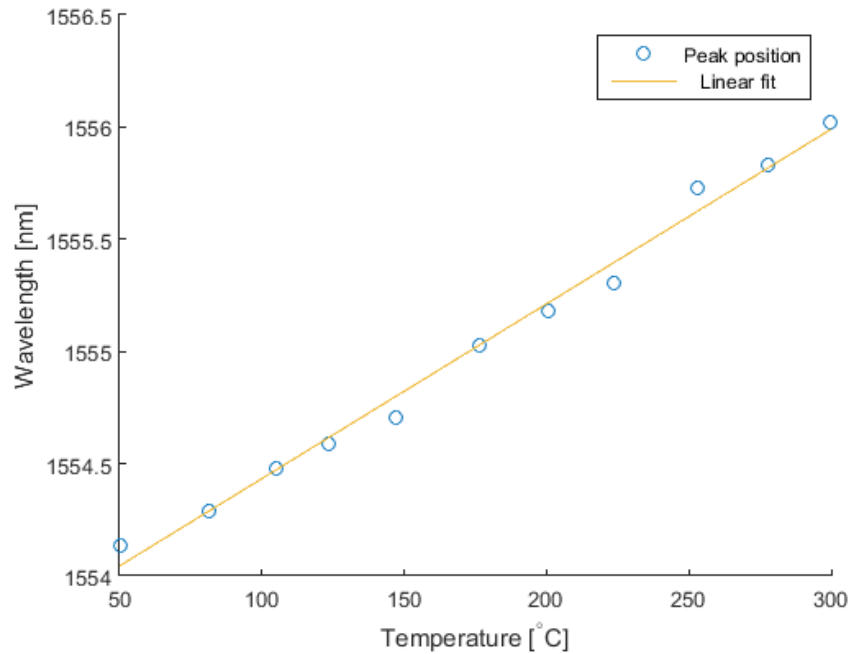
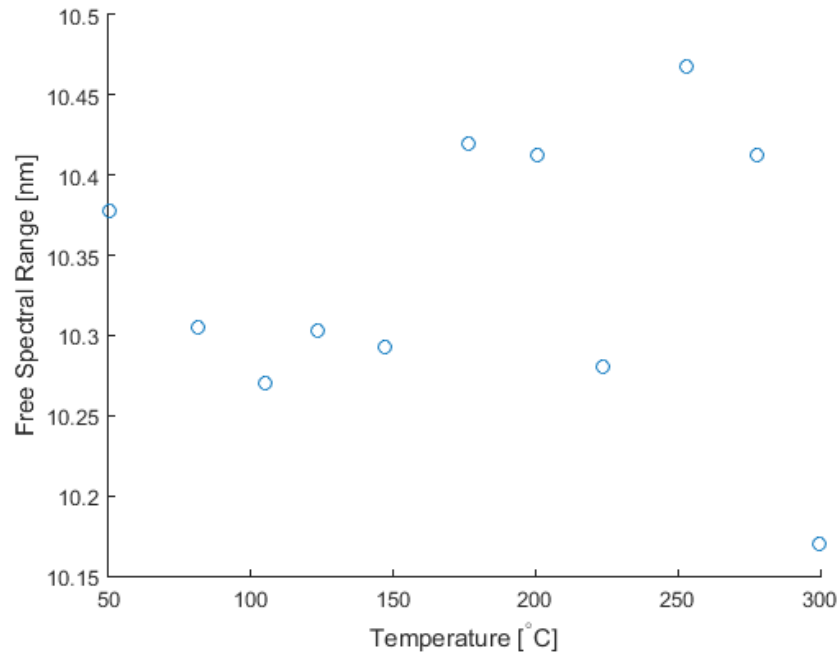


Figure 4.2 shows the linearity of the wavelength shift with temperature. The data is found from tracking one of the peaks as the temperature is increased. This relationship is also expressed in equation (2.14) which would affect the phase delay in (2.7) and subsequently the peak positions in (2.9). The linear fit has a norm of residuals close to .2, which means the fit is close to the data. The slope gives a sensitivity of $7.8 \text{ pm}/^\circ\text{C}$.

The FSR was also looked at for this data, however, no discernible shift was found. The FSR as a function of temperature is shown in Figure 4.3.

Figure 4.3: Temperature testing FSR results



No pattern was found when looking at the FSR between the peaks. Figure 4.3 shows a representative pattern when looking at the FSR between the third and fourth peaks in the spectrum.

Due to the relatively low temperature at which the fiber core bends, this sensor would work most efficiently at low temperatures.

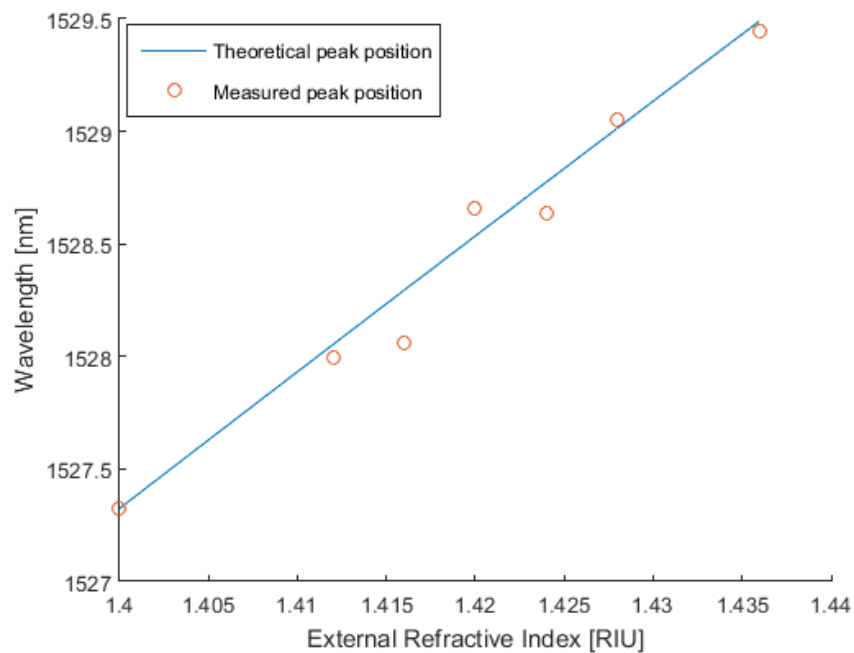
4.2 External Refractive Index Testing

This sensor's effectiveness at measuring the refractive index in the cavity was also tested. The refractive index of liquids can only be measured up to the refractive index of the core, which is 1.444 for silica at 1550 nm. If the refractive index is higher in the surrounding cavity than in the core, total internal reflection will no longer hold and the light is no longer

confined.

To test this phenomena, the sensor head is dipped in many different refractive index oils. A set of refractive index oils by Cargille Laboratories was used with indexes ranging from 1.4 to 1.436. With each trial, the sensor is first swirled in acetone to remove all excess debris or oil that may have been trapped in the cavity. Then, the sensor is dipped into the refractive index oil while connected to a CTS. It takes a couple of seconds for the spectrum to settle, but once it does the spectrum is averaged over 16 samples and saved. The results from this testing are shown in figure 4.4.

Figure 4.4: External refractive index testing results

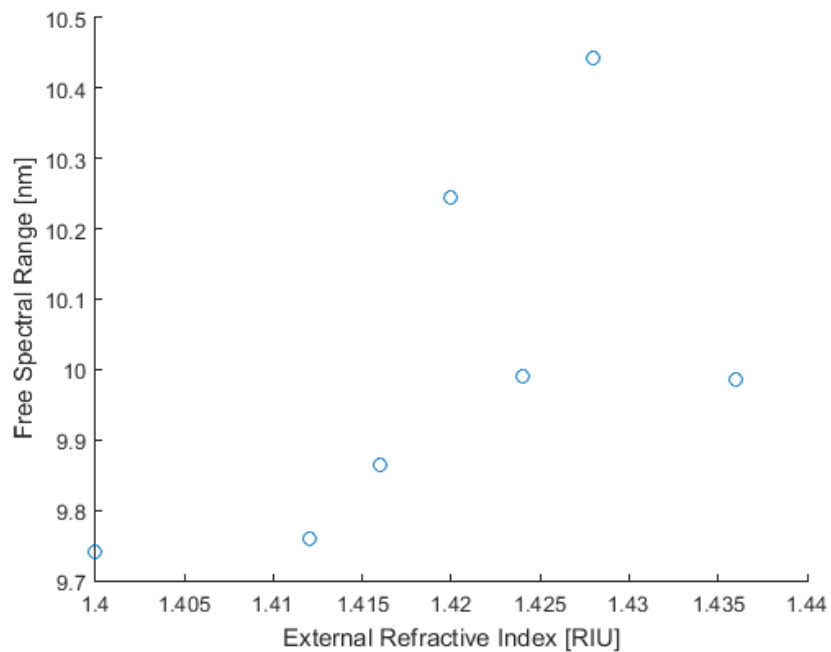


From equations (2.25) and (2.26) there is a relationship between the effective refractive index and the peak wavelengths of the spectrum. The figure above shows that the theoretical and measured results match quite well. The norm of residuals in this case is .3. There is a distinct linear relationship in the measured results. Based on the theoretical and measured

results, there is a sensitivity of $60 \text{ nm}/\text{RIU}$.

Similar to the temperature testing, however, when looking at the FSR for this test there is no pattern (Figure 4.5).

Figure 4.5: External refractive index FSR results



There seems to be a general increase in the FSR when the temperature is increased, but it does not seem to be governed by any specific function.

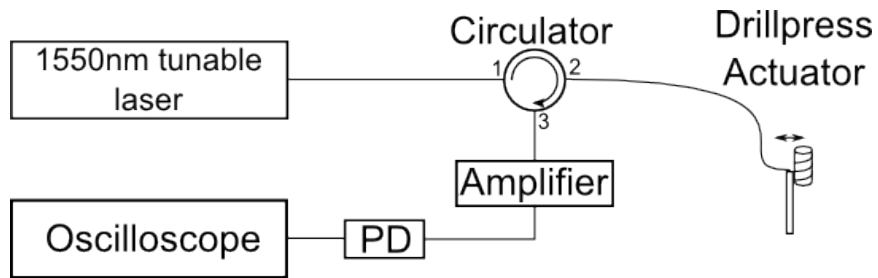
4.3 Axial Acceleration Testing

The acceleration of the fiber along its axis was tested. It was theorized that under axial acceleration the fiber core will compress or stretch based on the direction of acceleration. This, in turn, causes the length of the fiber core and, subsequently, the IFPI cavity to increase

or decrease. With the length of the cavity fluctuating, the spectrum will shift back and forth enough to be measured.

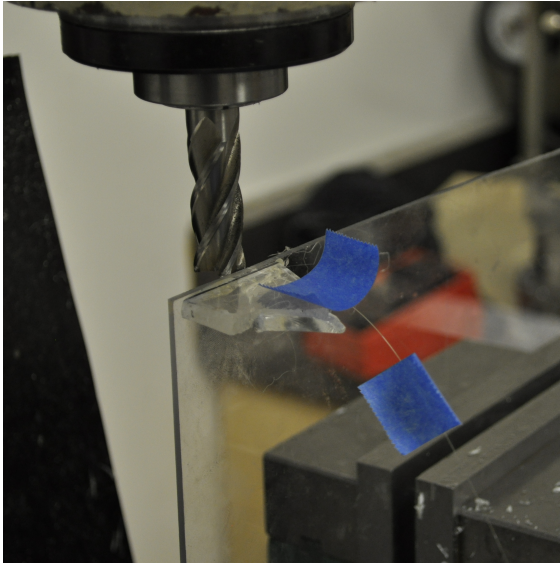
The system used to test out this theory is shown below in Figure 4.6.

Figure 4.6: Axial acceleration testing setup



A New Focus tunable laser (model number 6328) is used which has a wavelength range of 1520 nm to 1570 nm and a short linewidth of < 300 kHz. With such a large range, the laser is able to be tuned across the entire CTS spectrum bandwidth. The laser light is then fed into a polarization-maintaining circulator (Photonics, Inc. 800897) and guided to the actuator. The actuator is actually a drill press with the bit pressed against a piece of plastic. Photographs of the setup are shown in Figure 4.7.

Figure 4.7: Axial acceleration fiber placement



(a) Fiber placement with plastic sheet



(b) Close-up on sensor

The light is then reflected from the actuator back into the circulator and fed into a Nor-tel Networks Erbium-Doped Fiber Amplifier (EDFA). The output of this EDFA goes to a HP Lightwave Converter, a photodetector (PD), and then into a LeCroy WavePro 725Zi oscilloscope.

For testing, the wavelength 1540.6 nm was chosen to put the sensor in quadrature. In quadrature means that the interrogation wavelength is on the incline or decline part of the interrogated spectrum where the slope is highest and also highly linear. Therefore, when the spectrum shifts due to the acceleration the output into the oscilloscope will be maximum and can be assumed to be linear. The EDFA was set to 15dB of gain since the reflection of the sensor is low. The oscilloscope was set to take one second snapshots at 2.5 MS/s for high quality data. For the drill press actuator, a $\frac{5}{8}$ in auger drill bit was used which has four cutting grooves 1 mm deep when an object is laid flat across two consecutive teeth. Knowing the groove depth and RPM of the drill, the acceleration of the plastic sheet carrying the sensor can be calculated.

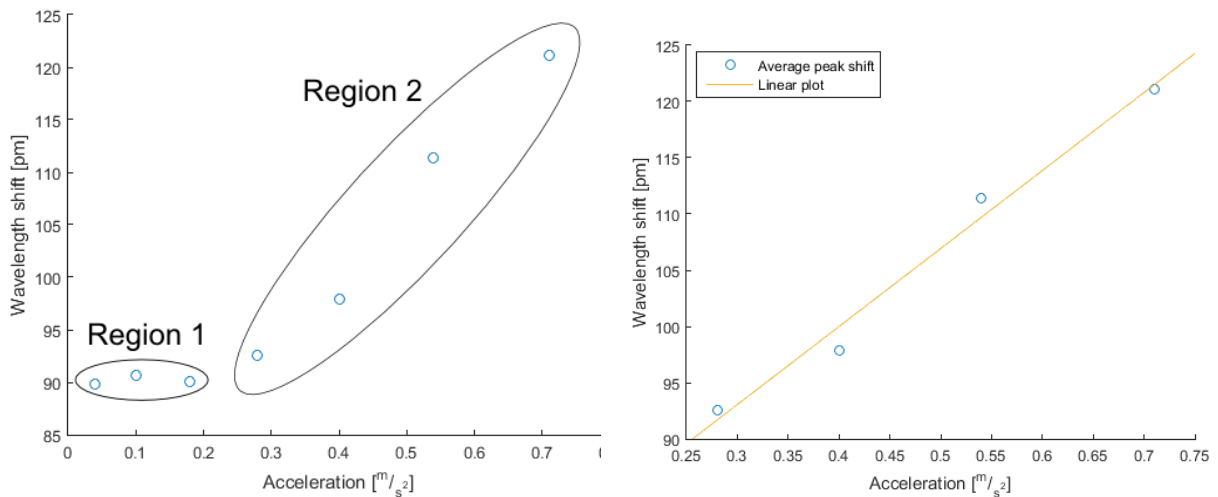
The acceleration can be calculated by the following method.

$$\begin{aligned}
 a &= \frac{\Delta v}{\Delta t} = \frac{\Delta x}{(\Delta t)^2} \\
 &= \frac{\Delta x}{(SPR/8)^2}
 \end{aligned}
 \tag{4.1}$$

where SPR is the seconds per revolution and the factor of 8 is because there are 4 teeth each with upward and downward accelerations.

In the testing, it was found that there are two distinct regions, labeled region 1 and region 2. Region 1 is where the drill was not at a high enough RPM and, therefore, acceleration for there to be a difference in the peaks of the returned signal. Region 2 is where there is clearly more of a trend line as the drill RPM, and therefore the acceleration, increases. The results are shown below in figure 4.8.

Figure 4.8: Axial vibration results



(a) Both regions

(b) Close-up on region 2

The PD gives an output in Volts. The oscilloscope records these values while AC coupled. Knowing that the responsivity of the PD is $300 V/w$, the wavelength shift can be found by

using the fact that the spectrum can be approximated to linear in the region and taking into account the gain from the EDFA. So, by taking the measured value and changing it into watts, the reflectance power change can be measured. From this power change, going back to the initial spectrum the wavelength shift can be discerned. Over region 1, a maximum wavelength shift of about 90 pm is observed below $.2 m/s^2$. In region 2, there is a linear relationship between the acceleration of the fiber and the shift in wavelength. Region 2 shows a sensitivity of $70 pm/unit\ of\ acceleration$ and has a norm of residuals of 2.85 meaning that the fit is fairly close. More data points would be needed to get a better fit. Examples of the spectrum for various RPM are listed in Appendix A. In these examples, multiple peaks per rotation are seen. This is because the plastic sheet hits the drill bit multiple times. For the higher acceleration trials, the multiple hits are dampened out faster leading to the plastic sheet hitting less before stabilizing.

The frequency spectrum of these plots are interesting, also given in Appendix A. They show that the repeated banging of the plastic sheet against the drill bit occurs at around 1.23 kHz and 1.3 kHz. These two frequencies are repeated in all of the spectrum for each RPM tested. Because of the dampening of the plastic as it rotates around the bit, the higher RPMs dampen faster and give higher frequencies as it does.

Chapter 5

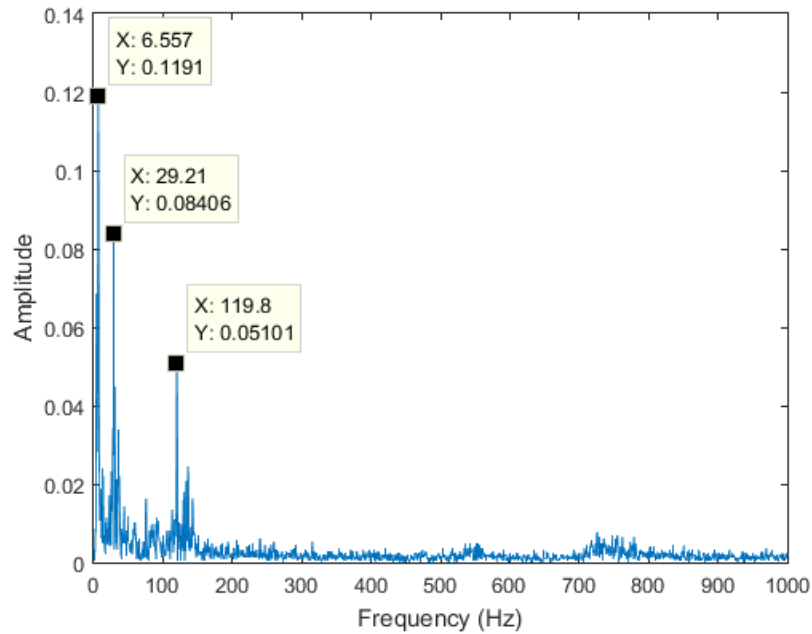
Future Work

5.1 Work done on Tangential Acceleration

The results of the axial acceleration testing are given in the previous chapter, but what happens when tangential acceleration is tested instead? This course of action was taken before the scope of the thesis was limited. Two tests were performed with this question: one using SMF looking at building vibrations and one using PMF to try to see the direction of the acceleration.

Starting with the first test, the fiber was placed on the floor of the Center for Photonics Technology in its machine room. The test setup is the same as was used in Figure 4.4 except that the actuator was the floor itself. The same steps were taken to procure the data and the FFT was taken of the data to see the resonances of the building. The FFT is shown in figure 5.1.

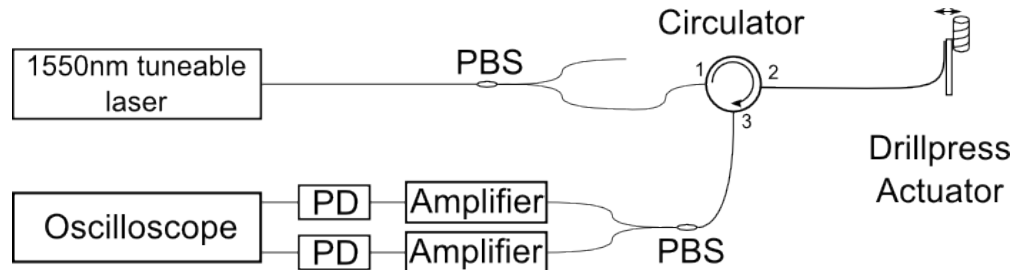
Figure 5.1: FFT of building vibrations



In this FFT spectrum, there are three observable peaks. Speculating, the peak at 6.6 Hz could be the natural frequency of the building and the other two could be from the HVAC equipment. This would be useful in finding frequencies to which a structure is most prone.

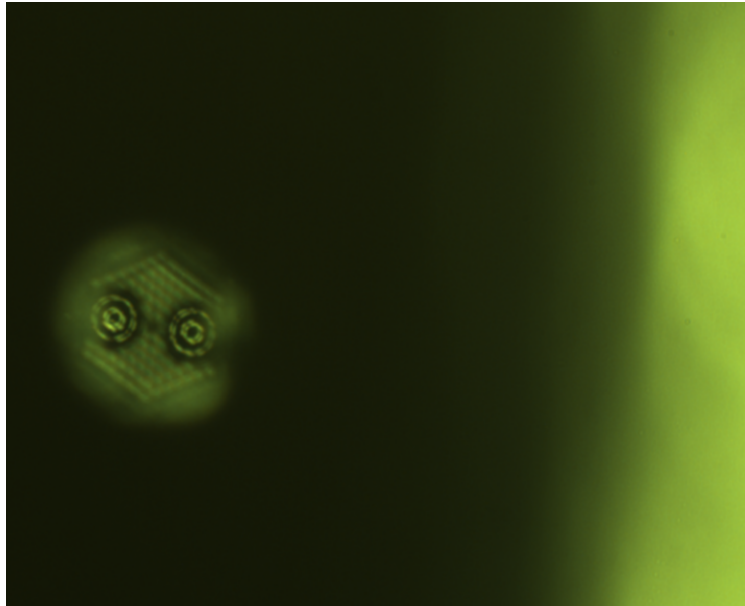
The second line of testing is to use a PMF as the lead-in fiber. By using one polarization to interrogate the sensor and watching both return polarizations, in theory the direction of acceleration can be obtained. The setup for this test is shown in figure 5.2.

Figure 5.2: Setup of tangential vibration test



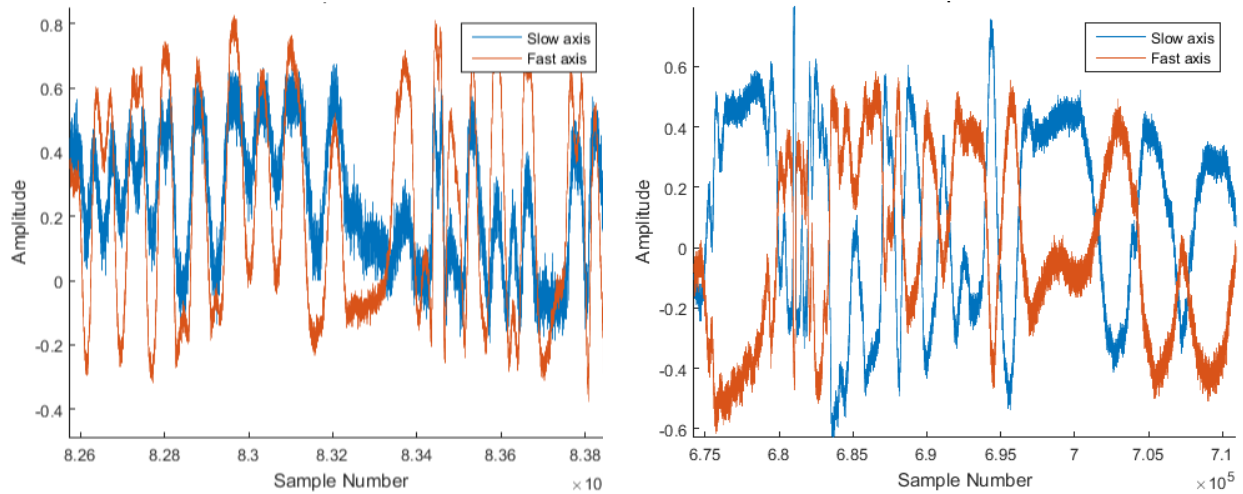
The test setup is similar to the SMF testing, however, polarization beam splitters (PBS) are added to only have one polarization enter the system from the laser and to split the polarizations so they can be viewed separately on the oscilloscope. The PBS that were used (General Photonics PB-15-P2- FC/APC) take the incoming light, place the slow mode into the slow mode of Port 1 and place the fast mode into the slow mode of Port 2. Therefore, the sensor is only interrogated on the slow mode. The reflected signal gets split once again and the oscilloscope records each polarization separately from each other. The sensor is then placed vertical on the plastic sheet and the test is run with the slow mode of the lead-in fiber normal to the axis of vibration, shown in figure 5.3.

Figure 5.3: Slow mode tangential to acceleration direction



This photograph shows the sensor tip when focused to the splicing point instead of the fiber end. The fiber is then rotated 90 degrees and the test is repeated. Some zoomed in portions of the results are shown below after normalization.

Figure 5.4: PMF tangential vibration results



(a) Results from 0deg rotation at 250rpm

(b) Results from 90deg rotation at 250rpm

As shown, rotating the axis of vibration also changes the amplitude difference between the two reflected modes. A full rotation of 90° reflects the fast axis over the amplitude axis. This can be used to tell which direction the acceleration is coming from by looking at the magnitude of each returning axis and their trend towards each other.

These two tasks were not completed further due to an inability to accurately describe the wavelength shifts of the spectrum. Originally, macrobending of the fiber was thought to facilitate the wavelength shifts, but that was proven wrong with the realization of how minimal a part it plays in shifting the spectrum. Therefore, the elongation and compression of the fiber due to this acceleration is the means by which the cavity length changes and the spectrum shifts. There may also be birefringence effects which shift the wavelength since the core acts like a cantilever beam and bends off of the fibers' axis.

5.2 Other areas to explore

Another possible direction to further take is to inscribe an FBG onto the PCF fiber tip. This would allow much higher reflections from the cavity and could potentially be characterized easier by the use of an FBG rather than an IFPI cavity. In this case, a photosensitive PCF fiber would need to be used with buffered HF so that the Ge doped core etched slower than the silica hole structure in which it is encased.

Chapter 6

Concluding Remarks

This work demonstrates the varied uses for this sensor structure. A small segment of PCF is spliced onto an SMF or PMF and etched out to form an IFPI cavity. This cavity has a free-standing core that acts as a cantilever beam. In responding to low temperature changes, refractive index variations and axial acceleration, the sensor followed linear paths that agreed with the theoretical predictions. The theory and calculations behind each test are presented and worked through. Future work is also discussed on steps that can be taken to improve upon the tangential acceleration measurements. There is also the possible path of writing an FBG into the PCF for stronger reflections. Both of these directions were out of the scope of this thesis.

With a versatile set of measuring capabilities, this sensor would be useful in a broad range of fields. Some examples would be in the bio-medical field with refractive index and temperature sensing, the civil field with building vibration measurements, and much more.

Bibliography

- [1] C. Menadier, C. Kissinger, and H. Adkins, “The fotonic sensor,” *Instruments and Control Systems*, vol. 40, no. 6, 1967.
- [2] Y. Zhao, J. Chang, J. Ni, Q. Wang, T. Liu, C. Wang, P. Wang, G. Lv, and G. Peng, “Novel gas sensor combined active fiber loop ring-down and dual wavelengths differential absorption method,” *Optics express*, vol. 22, no. 9, pp. 11244–11253, 2014.
- [3] E. Friebele, C. Askins, A. Bosse, A. Kersey, H. Patrick, W. Pogue, M. Putnam, W. Simon, F. Tasker, W. Vincent, *et al.*, “Optical fiber sensors for spacecraft applications,” *Smart materials and structures*, vol. 8, no. 6, p. 813, 1999.
- [4] E. Friebele, C. Askins, G. Miller, J. Peele, and L. Wasserman, “Optical fiber sensors for spacecraft: applications and challenges,” in *Optical Science and Technology, the SPIE 49th Annual Meeting*, pp. 120–131, International Society for Optics and Photonics, 2004.
- [5] K. Bohnert, P. Gabus, J. Kostovic, and H. Brändle, “Optical fiber sensors for the electric power industry,” *Optics and Lasers in Engineering*, vol. 43, no. 3, pp. 511–526, 2005.
- [6] F. Baldini, A. Giannetti, A. Mencaglia, and C. Trono, “Fiber optic sensors for biomedical applications,” *Current Analytical Chemistry*, vol. 4, no. 4, pp. 378–390, 2008.
- [7] J. Peterson and G. Vurek, “Fiber-optic sensors for biomedical applications,” *Science*, vol. 224, no. 4645, pp. 123–127, 1984.
- [8] A. Mignani and F. Baldini, “Biomedical sensors using optical fibres,” *Reports on Progress in Physics*, vol. 59, no. 1, p. 1, 1996.

- [9] B. Culshaw and A. Kersey, “Fiber-optic sensing: A historical perspective,” *Journal of lightwave technology*, vol. 26, no. 9, pp. 1064–1078, 2008.
- [10] C. Fabry and A. Perot, “Sur les franges des lames minces argentées et leur application à la mesure de petites épaisseurs d’air,” *Ann. Chim. Phys.*, vol. 12, pp. 459–501, 1897.
- [11] J. Mulligan, “Who were fabry and pérot?,” *American Journal of Physics*, vol. 66, no. 9, pp. 797–802, 1998.
- [12] B. Culshaw, “Optical fiber sensor technologies: opportunities and-perhaps-pitfalls,” *Journal of lightwave technology*, vol. 22, no. 1, p. 39, 2004.
- [13] K. Murphy, M. Gunther, A. Vengsarkar, and R. Claus, “Quadrature phase-shifted, extrinsic fabry–perot optical fiber sensors,” *Optics Letters*, vol. 16, no. 4, pp. 273–275, 1991.
- [14] Y. Rao, S. Yuan, X. Zeng, D. Lian, Y. Zhu, Y. Wang, S. Huang, T. Liu, G. Fernando, L. Zhang, *et al.*, “Simultaneous strain and temperature measurement of advanced 3-d braided composite materials using an improved efpi/fbg system,” *Optics and Lasers in Engineering*, vol. 38, no. 6, pp. 557–566, 2002.
- [15] T. Lü and S. Yang, “Extrinsic fabry-perot cavity optical fiber liquid-level sensor,” *Applied optics*, vol. 46, no. 18, pp. 3682–3687, 2007.
- [16] D. Kim, F. Shen, X. Chen, and A. Wang, “Simultaneous measurement of refractive index and temperature based on a reflection-mode long-period grating and an intrinsic fabry-perot interferometer sensor,” *Optics letters*, vol. 30, no. 22, pp. 3000–3002, 2005.
- [17] T. Kao and H. Taylor, “High-sensitivity intrinsic fiber-optic fabry–perot pressure sensor,” *Optics letters*, vol. 21, no. 8, pp. 615–617, 1996.
- [18] X. Wang, J. Xu, Z. Wang, K. L. Cooper, and A. Wang, “Intrinsic fabry-perot interferometer with a micrometric tip for biomedical applications,” in *Bioengineering Conference, 2006. Proceedings of the IEEE 32nd Annual Northeast*, pp. 55–56, IEEE, 2006.

- [19] X. Wan and H. Taylor, "Intrinsic fiber fabry-perot temperature sensor with fiber bragg grating mirrors," *Optics letters*, vol. 27, no. 16, pp. 1388–1390, 2002.
- [20] Y. Rao, P. Henderson, D. Jackson, L. Zhang, and I. Bennion, "Simultaneous strain, temperature and vibration measurement using a multiplexed in-fibre-bragg-grating/fibre-fabry-perot sensor system," *Electronics letters*, vol. 33, no. 24, pp. 2063–2064, 1997.
- [21] C. Lee, R. Atkins, and H. Taylor, "Performance of a fiber-optic temperature sensor from -200 to 1050c," *Optics letters*, vol. 13, pp. 1038–1040, 1988.
- [22] W. Tsai and C. Lin, "A novel structure for the intrinsic fabry-perot fiber-optic temperature sensor," *Journal of Lightwave Technology*, vol. 19, no. 5, p. 682, 2001.
- [23] R. Hyspzer, J. Plucinski, and H. J. Wierzba, "Optical fibre temperature sensor based on a blackbody radiation," in *Optical Fibers and Their Applications V*, pp. 476–479, International Society for Optics and Photonics, 1990.
- [24] M. A. Farahani and T. Gogolla, "Spontaneous raman scattering in optical fibers with modulated probe light for distributed temperature raman remote sensing," *Journal of Lightwave Technology*, vol. 17, no. 8, p. 1379, 1999.
- [25] Z. Zhang, K. Grattan, and A. Palmer, "Fiber-optic high-temperature sensor based on the fluorescence lifetime of alexandrite," *Review of scientific Instruments*, vol. 63, no. 8, pp. 3869–3873, 1992.
- [26] W. B. Ji, H. H. Liu, S. C. Tjin, K. K. Chow, and A. Lim, "Ultrahigh sensitivity refractive index sensor based on optical microfiber," *Photonics Technology Letters, IEEE*, vol. 24, no. 20, pp. 1872–1874, 2012.
- [27] V. Bhatia and A. M. Vengsarkar, "Optical fiber long-period grating sensors," *Optics Letters*, vol. 21, no. 9, pp. 692–694, 1996.
- [28] D. K. Wu, B. T. Kuhlmeiy, and B. J. Eggleton, "Ultrasensitive photonic crystal fiber refractive index sensor," *Optics letters*, vol. 34, no. 3, pp. 322–324, 2009.

- [29] Y. Rao, “Absolute strain measurement using an in-fibre-bragg-grating-based fabry-perot sensor,” *Electronics Letters*, vol. 36, no. 8, pp. 708–709, 2000.
- [30] E. Pinet, E. Cibula, and D. DJ, “Ultra-miniature all-glass fabry-pérot pressure sensor manufactured at the tip of a multimode optical fiber,” in *Optics East 2007*, pp. 67700U–67700U, International Society for Optics and Photonics, 2007.
- [31] S. Pevec and D. Donlagic, “All-fiber, long-active-length fabry-perot strain sensor,” *Optics express*, vol. 19, no. 16, pp. 15641–15651, 2011.
- [32] Y. Rao, T. Zhu, X. Yang, and D. Duan, “In-line fiber-optic etalon formed by hollow-core photonic crystal fiber,” *Optics letters*, vol. 32, no. 18, pp. 2662–2664, 2007.
- [33] J. Villatoro, V. Finazzi, G. Coviello, and V. Pruneri, “Photonic-crystal-fiber-enabled micro-fabry-perot interferometer,” *Optics letters*, vol. 34, no. 16, pp. 2441–2443, 2009.
- [34] L. Xu, M. Deng, D. Duan, W. Wen, and M. Han, “High-temperature measurement by using a pcf-based fabry-perot interferometer,” *Optics and Lasers in Engineering*, vol. 50, no. 10, pp. 1391–1396, 2012.
- [35] R. Wang and X. Qiao, “Intrinsic fabry-perot interferometric sensor based on microfiber created by chemical etching,” *Sensors*, vol. 14, no. 9, pp. 16808–16815, 2014.
- [36] R. Wang and X. Qiao, “Micro fabry-perot interferometer based on suspended core created by etching microstructure fiber,” in *OFS2014 23rd International Conference on Optical Fiber Sensors*, pp. 915780–915780, International Society for Optics and Photonics, 2014.
- [37] R. Wang, M. Fraser, J. Li, X. Qiao, and A. Wang, “Integrated in-fiber coupler for microsphere modes resonator excitation,” *Optics Letters*, vol. 40, no. 3, pp. 308–311, 2015.

- [38] T. Guo, Q. Zhao, Q. Dou, H. Zhang, L. Xue, G. Huang, and X. Dong, “Temperature-insensitive fiber bragg grating liquid-level sensor based on bending cantilever beam,” *Photonics Technology Letters, IEEE*, vol. 17, no. 11, pp. 2400–2402, 2005.
- [39] T. Bailey and J. Ubbard, “Distributed piezoelectric-polymer active vibration control of a cantilever beam,” *Journal of Guidance, Control, and Dynamics*, vol. 8, no. 5, pp. 605–611, 1985.
- [40] F. Battiston, J. Ramseyer, H. Lang, M. Baller, C. Gerber, J. Gimzewski, E. Meyer, and H. Güntherodt, “A chemical sensor based on a microfabricated cantilever array with simultaneous resonance-frequency and bending readout,” *Sensors and Actuators B: Chemical*, vol. 77, no. 1, pp. 122–131, 2001.
- [41] S. Theriault, K. O. Hill, F. Bilodeau, D. Johnson, J. Albert, G. Drouin, and A. Béliveau, “High-g accelerometer based on an in-fiber bragg grating sensor,” *Optical Review*, vol. 4, no. 1, pp. A145–A147, 1997.
- [42] W. Zhang, X. Dong, Q. Zhao, G. Kai, and S. Yuan, “Fbg-type sensor for simultaneous measurement of force (or displacement) and temperature based on bilateral cantilever beam,” *Photonics Technology Letters, IEEE*, vol. 13, no. 12, pp. 1340–1342, 2001.
- [43] T. Gangopadhyay, “Prospects for fibre bragg gratings and fabry-perot interferometers in fibre-optic vibration sensing,” *Sensors and Actuators A: Physical*, vol. 113, no. 1, pp. 20–38, 2004.
- [44] J. Kalenik and R. Pajgk, “A cantilever optical-fiber accelerometer,” *Sensors and Actuators*, vol. 68, pp. 350–355, 1998.
- [45] A. Malki, P. Lecoy, J. Marty, C. Renouf, and P. Ferdinand, “Optical fiber accelerometer based on a silicon micromachined cantilever,” *Applied optics*, vol. 34, no. 34, pp. 8014–8018, 1995.

- [46] T. Yoshino, K. Kurosawa, K. Itoh, and T. Ose, “Fiber-optic fabry-perot interferometer and its sensor applications,” *Microwave Theory and Techniques, IEEE Transactions on*, vol. 30, no. 10, pp. 1612–1621, 1982.
- [47] R. Kist, S. Ramakrishnan, and H. Wolfelschneider, “The fiber fabry-perot and its applications as a fiber-optic sensor element.,” in *1985 International Technical Symposium/Europe*, pp. 126–135, International Society for Optics and Photonics, 1986.
- [48] T. A. Birks, J. C. Knight, and P. S. J. Russell, “Endlessly single-mode photonic crystal fiber,” *Optics letters*, vol. 22, no. 13, pp. 961–963, 1997.
- [49] W. Tsai and C. Lin, “A novel structure for the intrinsic fabry-perot fiber-optic temperature sensor,” *Journal of Lightwave Technology*, vol. 19, no. 5, p. 682, 2001.
- [50] D. Gloge, “Weakly guiding fibers,” *Applied Optics*, vol. 10, no. 10, pp. 2252–2258, 1971.
- [51] Corning, “An overview of macrobending and microbending of optical fibers,” 2010.
- [52] D. Monk, “A review of the chemical reaction mechanism and kinetics for hydrofluoric acid etching of silicon dioxide for surface micromachining applications,” *Thin Solid Films*, vol. 232, no. 1, pp. 1–12, 1993.

Appendix A

Axial vibration testing

Figure A.1: Axial vibration at 50 RPM

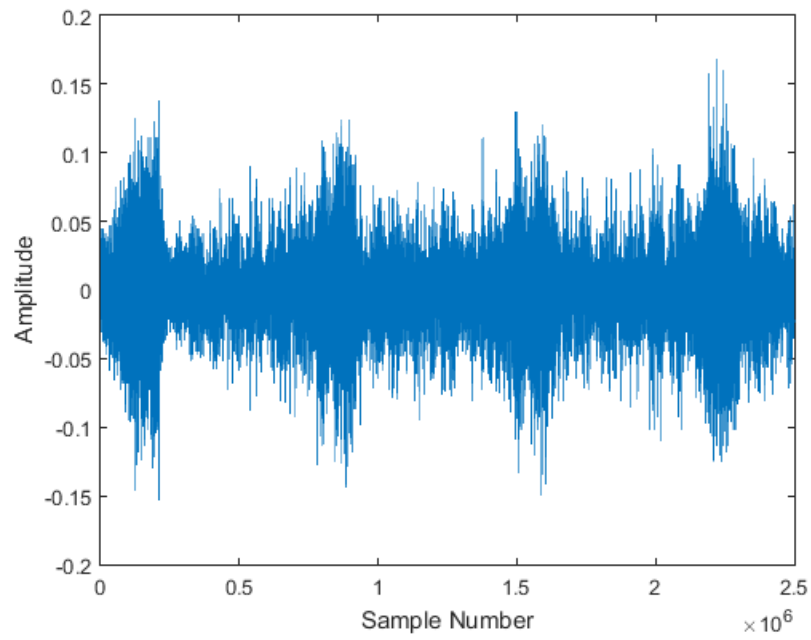


Figure A.2: Spectrum of axial vibration at 50 RPM

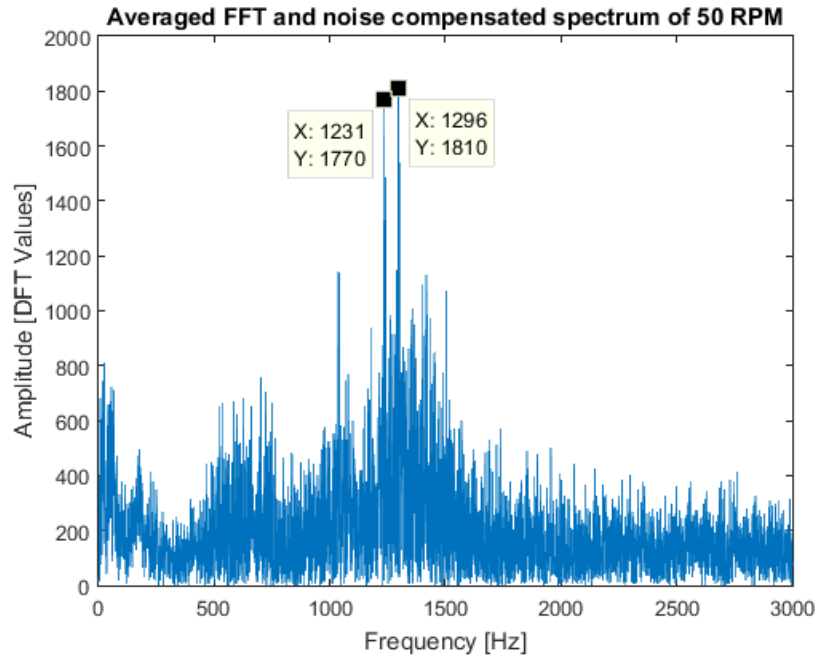


Figure A.3: Axial vibration at 75 RPM

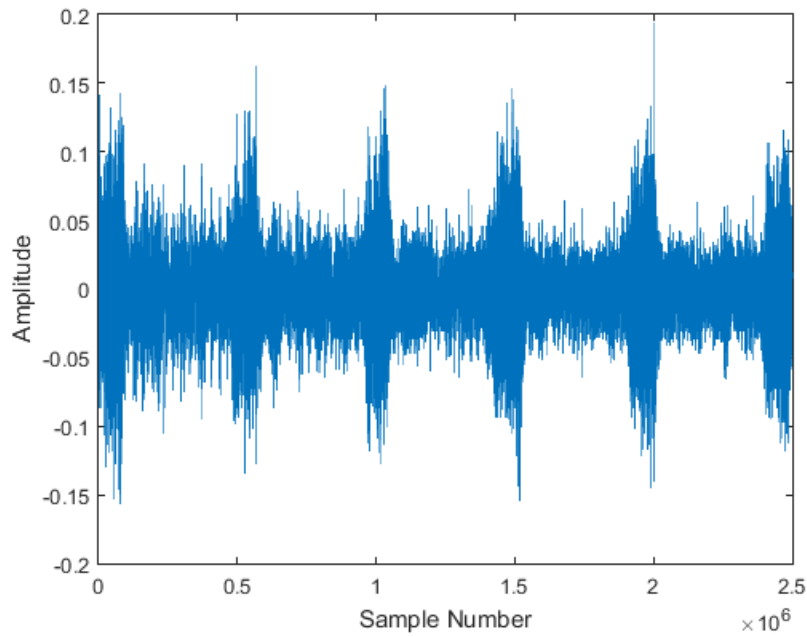


Figure A.4: Spectrum of axial vibration at 75 RPM

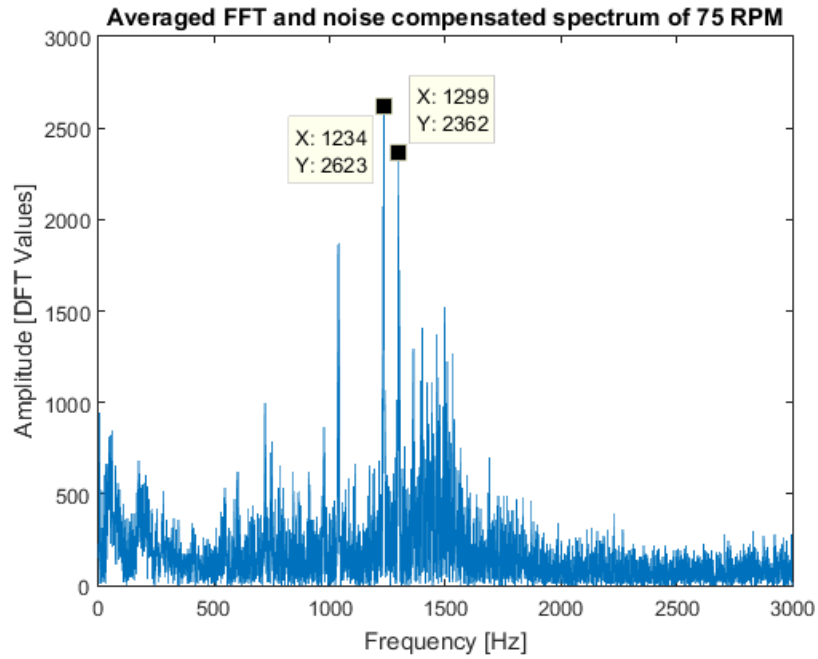


Figure A.5: Axial vibration at 100 RPM

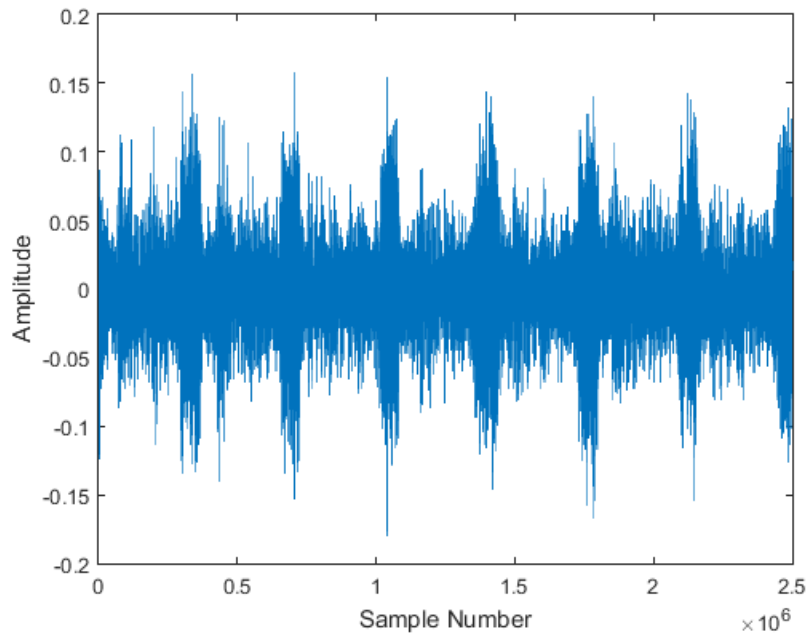


Figure A.6: Spectrum of axial vibration at 100 RPM

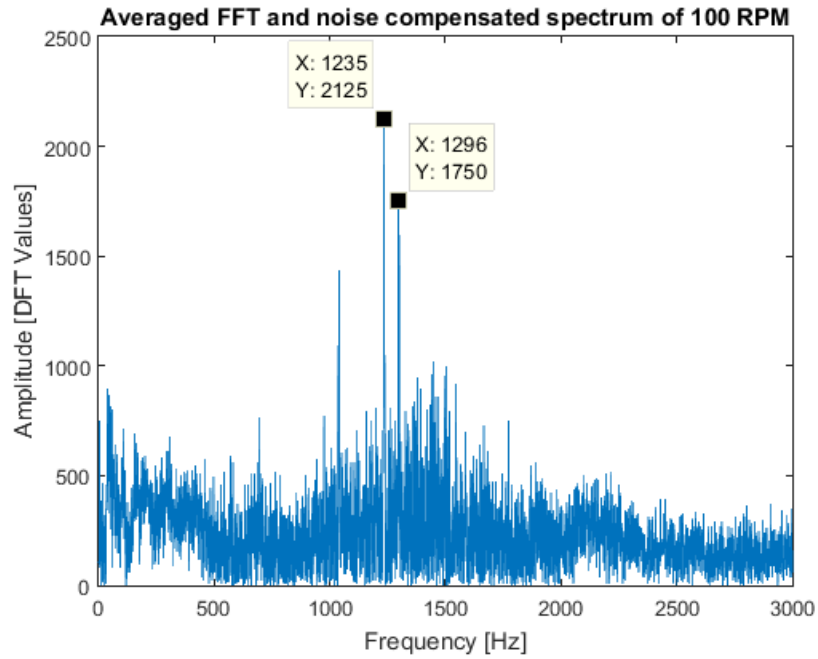


Figure A.7: Axial vibration at 125 RPM

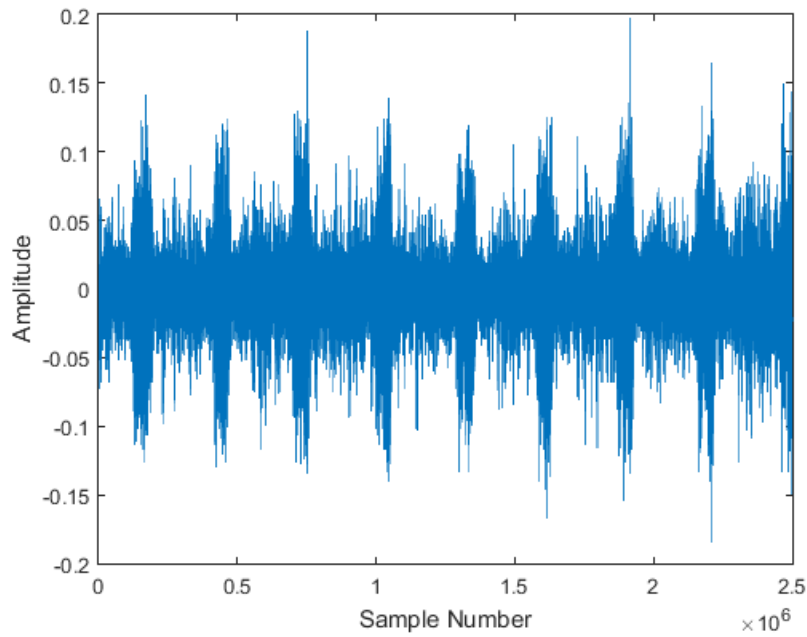


Figure A.8: Spectrum of axial vibration at 125 RPM

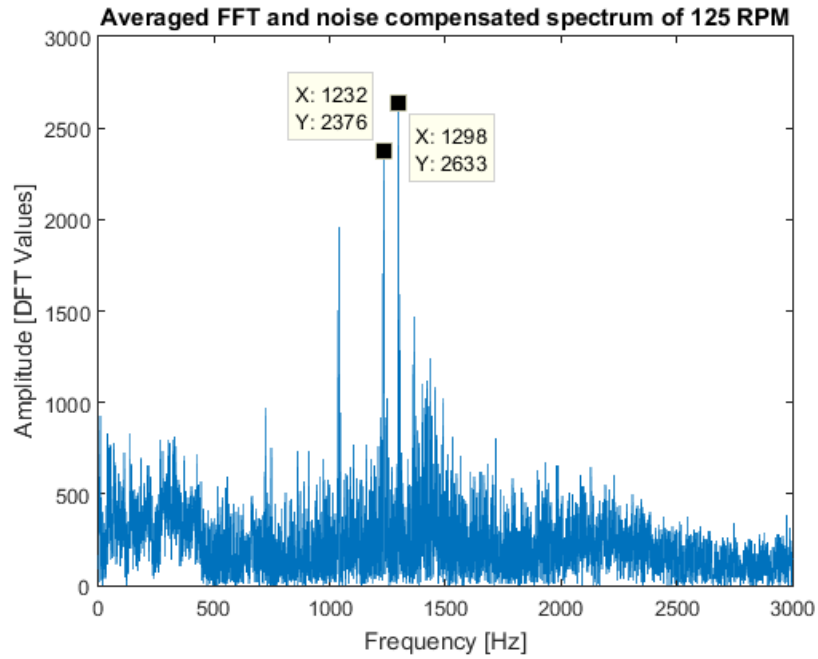


Figure A.9: Axial vibration at 150 RPM

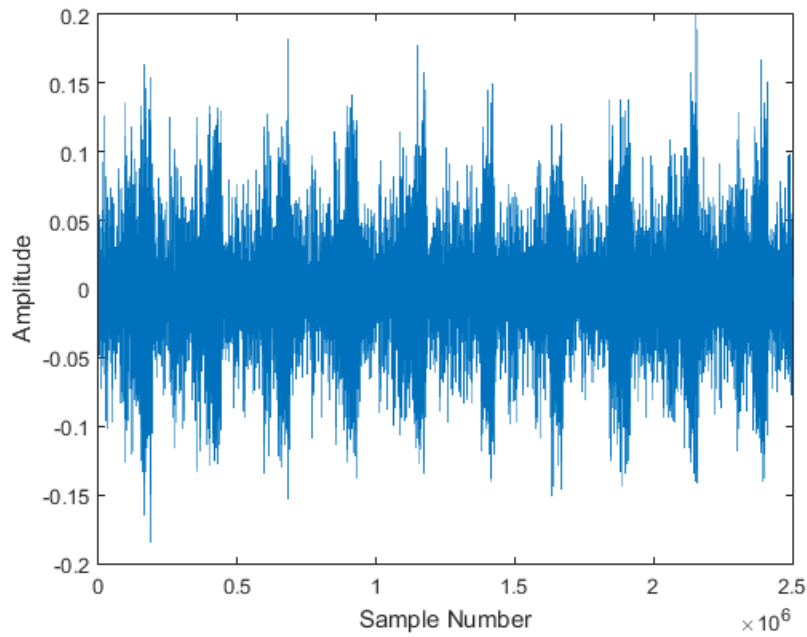


Figure A.10: Spectrum of axial vibration at 150 RPM

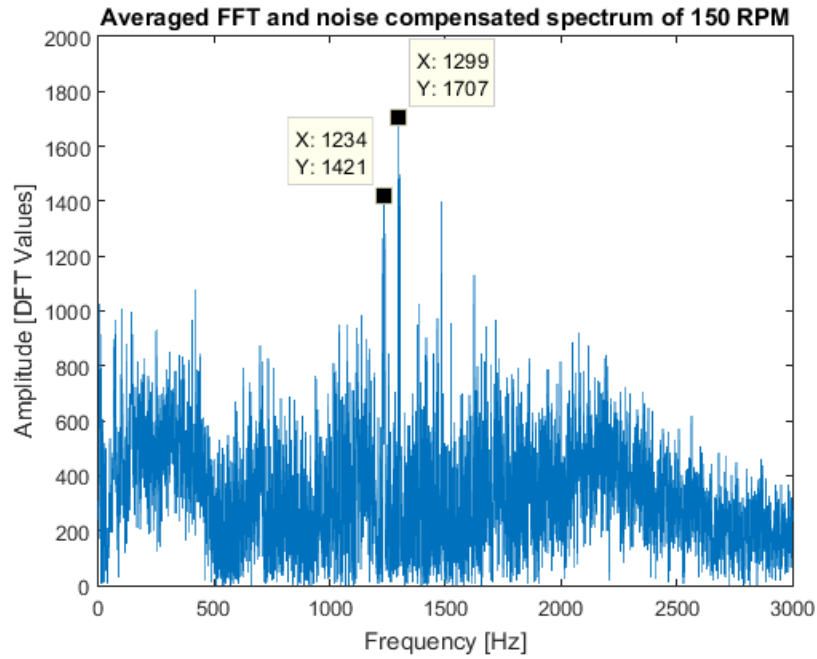


Figure A.11: Axial vibration at 175 RPM

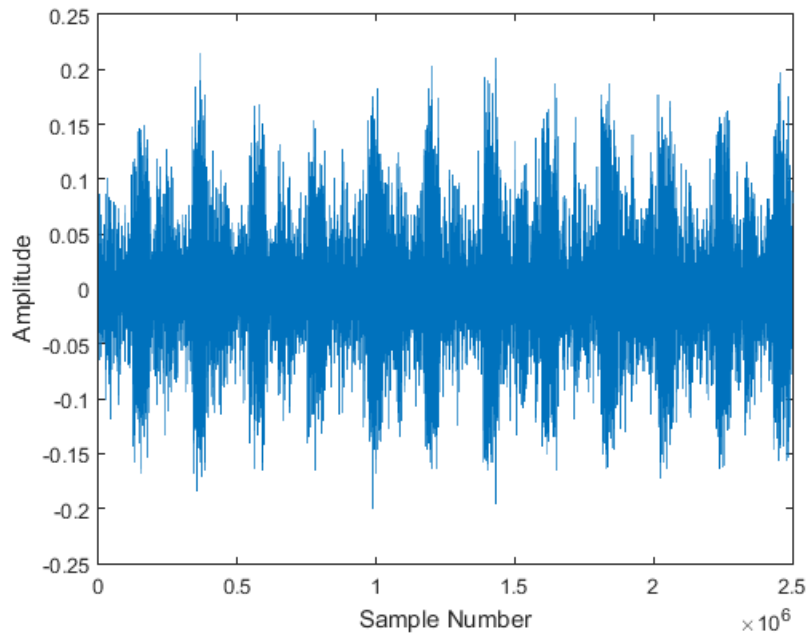


Figure A.12: Spectrum of axial vibration at 175 RPM

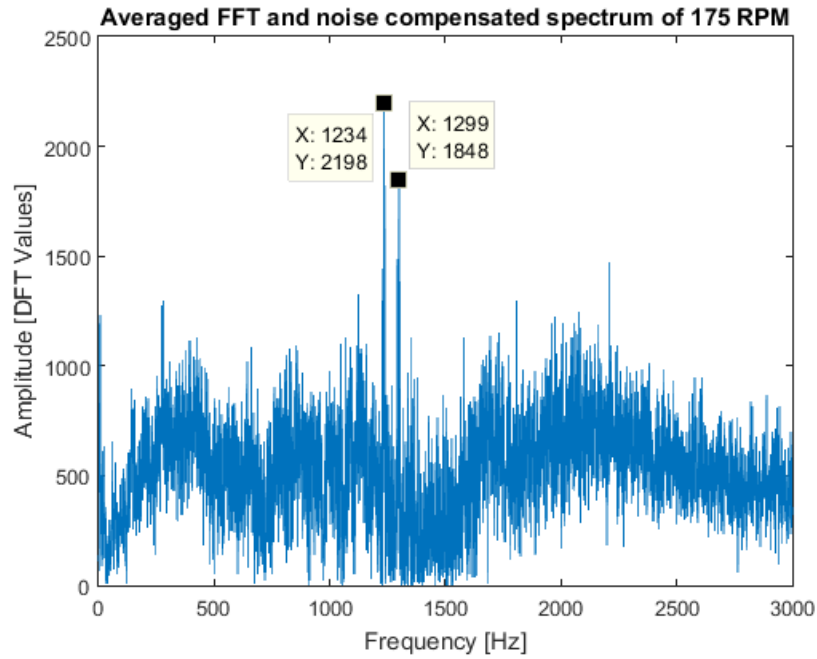


Figure A.13: Axial vibration at 200 RPM

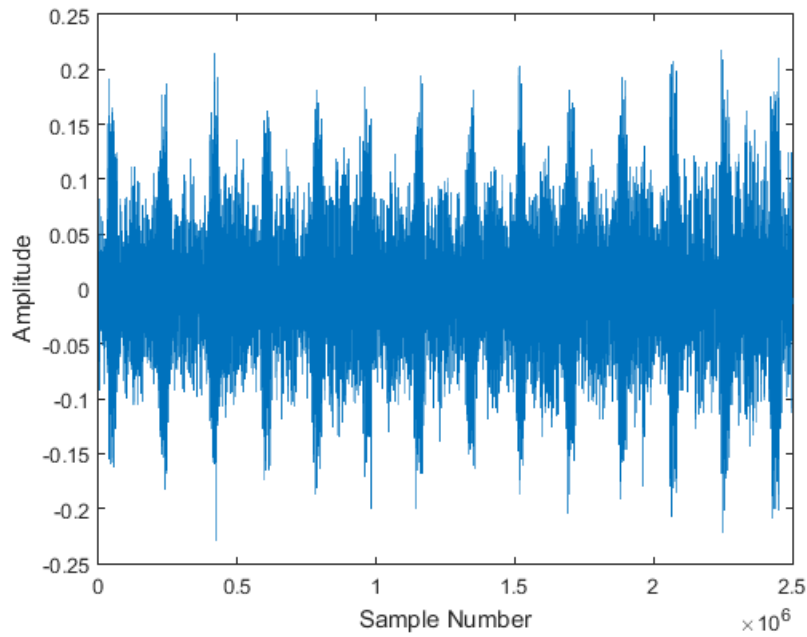


Figure A.14: Spectrum of axial vibration at 200 RPM

